Wintertime Aerosol Measurements during the Chilean Coastal Orographic Precipitation Experiment

Sara Lynn Fults [1]

Adam K. Massmann [2]

Aldo Montecinos [3]

Elisabeth Andrews [4, 5]

David E. Kingsmill [5]

Justin R. Minder [2]

Rene´ D. Garreaud [6]

Jefferson R. Snider [1, 7]

[1] University of Wyoming, Laramie, WY

[2] University at Albany, Albany, NY

[3] Universidad de Concepción, Concepción, Chile

[4] NOAA ESRL Global Monitoring Division, Boulder, CO

[5] University of Colorado, Boulder, CO

[6] Universidad de Chile, Santiago, Chile

[7] Corresponding Author

Abstract

The Chilean Coastal Orographic Precipitation Experiment (CCOPE) was a three-month field campaign (June, July and August 2015) that investigated wintertime coastal rain events. Reported here are analyses of aerosol measurements made at a coastal site during CCOPE. The aerosol monitoring site was located near Arauco, Chile. Aerosol number concentrations and aerosol size distributions were acquired with a Condensation Particle Counter (CPC) and an Ultra High Sensitivity Aerosol Spectrometer (UHSAS). Arauco CPC data were compared to values measured at the NOAA observatory Trinidad Head (THD) on the North Pacific Coast of California. The winter-averaged CPC concentration at Arauco is 2971 cm^{-3} ± 1802 cm^{-3}; at THD the average is 1059 cm^{-3} ± 855 cm^{-3}. Despite the typically more pristine Southern Pacific region, the Arauco average is larger than at THD ($p < 0.01$). Aerosol size distributions acquired during episodes of onshore flow were analyzed with Köhler theory and used to parameterize cloud condensation nuclei activation spectra. In addition, sea salt aerosol (SSA) concentration was parameterized as a function of sea surface wind speed. It is anticipated these parameterizations will be applied in modeling of wintertime Chilean coastal precipitation.

1 Introduction

Forecast error due to incomplete understanding of atmospheric aerosols is evident in the predictions of many atmospheric models. As an example, general circulation models (GCMs) are used to forecast the Earth system's response to emissions of both aerosols and greenhouse gases. In spite of several decades of GCM development, the effect of aerosols on future climate remains uncertain (Boucher et al. 2013), particularly when compared to the greater certainty in climate forcing from anthropogenic greenhouse gases (e.g., Hansen 2009, his Fig. 10).

Aerosols perturb the abundance of cloud droplets and rain drops within clouds warmer than 0 ^{o}C (liquid-only clouds). Consequently, upward reflection of solar radiation by liquid-only clouds (Twomey 1974), and upward reflection attributable to cloud fractional coverage (Albrecht 1989), increase with increased aerosol abundance. Commonly referred to as aerosol indirect effects on climate, these processes decrease the amount of solar energy absorbed by the Earth system, and thus oppose global warming due to greenhouse gases. Other aerosol indirect effects, for example those due to aerosols nucleating ice in mixed-phase clouds (McCoy et al., 2014), augment greenhouse gas warming.

Because of its lower population and lower intensity of anthropogenic aerosol emissions, the Southern Hemisphere has been explored as a region for conducting studies of aerosol indirect effects and for exploring contrasts with the Northern Hemisphere (Schwartz, 1988). This study contributes to previous investigations of Southern Hemispheric aerosols during winter (Gras, 1990; Gras 1995; Yum and Hudson 2004). We emphasize the following topics: 1) The parameterized relationship between sea salt aerosol (SSA) particles (diameter > 0.5 μm) and wind speed; 2) The role as cloud condensation nuclei (CCN) of particles that are both smaller and more numerous than the above-mentioned SSA; 3) The parameterized relationship

describing CCN activation spectra (Rogers and Yau, 1989; chapter 6), and 4) the potential application of the SSA and CCN parameterizations in numerical modelling of wintertime Southern Hemispheric clouds and precipitation. Motivating our investigation are modeling studies (Feingold et al. 1999), and analyses of field measurements (Gerber and Frick 2012), indicating that the reduction of rainfall due to increased CCN can be negated by SSA particles.

Measurements made with a Condensation Particle Counter (CPC), an instrument that reports the concentration of particles with diameter (D) larger than ~ 0.01 μm, have formed the basis of many previous investigations of aerosol abundance (Gras 1990; Brechtel et al. 1998; Dall'Osto et al. 2009; Andreae 2009). These studies also evaluated air parcel back trajectories and demonstrated that marine source regions are characterized by distinctly smaller concentrations than continental regions. Measurements of aerosol size distributions (ASDs) can also aid understanding of the contrast between marine and continental conditions (Brechtel et al. 1998; Birmili et al. 2001; Raes et al. 1997). The latter studies investigated accumulation mode particles, centered at ~ 0.1 μm, and particles sizing in a mode at a distinctly smaller central diameter (~ 0.05 μm). This smaller mode is commonly referred to as the Aitken mode. In marine settings, the coexistence of both modes has been attributed to in-cloud conversion of gas-phase sulfur dioxide (SO_2) to aerosol-phase sulfate (Hoppel et al. 1994), to coalescence scavenging occurring within clouds (Hudson et al. 2015), and to new particle formation (Covert et al. 1992; Petters et al. 2006). The latter process occurs in environments with sufficiently enhanced ratios of SO_2 relative to aerosol.

The present work is an analysis of CPC and ASD measurements acquired at a coastal site on the Central Chilean Pacific coast during the Southern Hemisphere winter (June, July, and August). Aerosol measurements were made during the Chilean Coastal Orographic Precipitation

Experiment (CCOPE) of 2015. CCOPE investigated aerosol properties and coastal orographic precipitation and meteorology (Massmann et al. 2017).

This paper is organized into the following sections: Section 2 has descriptions of the aerosol and meteorological instruments used to make surface measurements during CCOPE, and Sect. 3 describes our analysis methods. Section 4 includes four topics: 1) Analysis of CPC measurements and comparison to Coastal North Pacific measurements, 2) development of a relationship between size-integrated aerosol concentration and size-integrated aerosol volume, and comparison to similar relationships derived for summertime stratocumulus regimes, 3) development of a parameterization of CCN activation spectra, and 4) development of a parameterization of SSA number concentration. In Sect. 5, we compare our findings to previous work, and in Sect. 6 we conclude with an outlook for how our parameterizations could be applied in modeling of wintertime Central Chilean Pacific coast clouds and precipitation.

2 Measurements

2.1 Measurement Site

During CCOPE, a CPC (model 3010; TSI 2000a) and an Ultra High Sensitivity Aerosol Spectrometer (UHSAS) (DMT 2013) were operated at a residence (37.25° S, 73.34° W, 55 m above mean sea level (MSL)) near Arauco, Chile (population 35,000). Arauco is a coastal town on the Central Chilean Pacific coast. Our measurement site, hereafter the Arauco Site (Fig. 1), was selected because of our aim to characterize aerosols advecting onto South America from the Southeast Pacific. Related to this, our measurements were coordinated with investigations of rainfall inside the domain portrayed in Fig. 1. This study region lies in the South Pacific winter storm track and rainfall here can be strongly enhanced by the Nahuelbuta Mountains (Garreaud

et al. 2016; Massmann et al. 2017). During CCOPE, several rainfall events were studied using profiling radars and a precipitation disdrometer deployed at Curanilahue (Fig. 1), and a network of precipitation gauges. The Arauco Site is located on a forested hill; most of the population of Arauco lives east of the Arauco Site at an elevation less than 20 m MSL.

Salient characteristics of the CPC and UHSAS are provided in Table 1. These instruments were operated inside the residence at the Arauco Site. In addition, a 3-meter meteorological tower was deployed adjacent to the residence. Thermodynamic state (i.e., T, P, and humidity) and horizontal wind speed and direction were measured on the tower. CPC and meteorological measurements (minus wind direction) were acquired from 29 May to 14 August (Table 1), UHSAS measurements were acquired from 29 May to 28 June (Table 1), and wind direction measurements were acquired from 19 June to 14 August.

2.2 Instrumentation

Here we discuss characteristics of the CPC and UHSAS, sampling of the ambient CCOPE aerosol, data acquisition of CPC and UHSAS measurements during CCOPE, and use of the recorded UHSAS histograms to calculate ASDs. Additional information about the UHSAS is provided in Appendix A. In that appendix we discuss how we validated, in a laboratory, the UHSAS's determination of test aerosol concentration and particle size. During those validation studies we intentionally dried the test aerosols to a relative humidity (RH) $\leq$ 15%. Consequently, the effect of aerosol-bound water on either the physical size or the refractive index of the test particles was negligible. UHSAS sizing of partially dried haze droplets ($RH \leq 60$ %), sampled from the ambient atmosphere during CCOPE, and an associated particle size overestimate, is also discussed in Appendix A. In Appendix A, we estimate the particle size overestimate to be ~ 20 %.

During CCOPE, the CPC and UHSAS sampled ambient aerosol through a section of copper tube (length = 3 m, inner diameter = 0.003 m, volumetric flow rate = 34 cm^3 s^{-1}). The inlet end of the tube (hereafter, the sample tube) was secured below an eave on the west side of the residence at the Arauco Site. The Reynolds number (*Re*) of the flow within the sample tube was 960 and thus well below the value (*Re* = 2300) where laminar flow changes to turbulent flow. Particle transmission efficiencies were evaluated using Eq. (7.29) in Hinds (1999). These are 78% for $D = 0.01$ μm particles and ≥ 99% for $D = 0.1$ μm and $D = 1$ μm particles.

The CPC counts particles larger than $D = 0.012$ μm (Table 1) [1] up to a maximum concentration of 10,000 cm^{-3}. The UHSAS measures scattering produced when aerosol particles are drawn through light emitted by a solid state laser ($\lambda = 1.05$ μm). By reference to a calibration table (Cai et al. 2008; Cai et al. 2013), the UHSAS microprocessor converts scattered light intensity to particle size and accumulates the derived sizes in a 99 channel histogram. Channel widths are logarithmically uniform ($\Delta \log_{10} D = 0.013$) over the instrument's full range ($0.055 < D < 1.0$ μm). UHSAS data were recorded every 10 seconds and CPC data were recorded once per second (Table 1).

Eq. (1) was used to calculate the ASD.

$$\left(\frac{dN}{d\log_{10} D}\right)_i = \frac{\Delta n_i}{\dot{V} \cdot \Delta t \cdot \Delta \log_{10} D} \qquad (1)$$

Here Δn_i is the "i th" component of the count histogram and $\dot{V}$ is the aerosol flowrate. During CCOPE, the UHSAS aerosol flow rate and the particle count histogram were recorded once every ten seconds (Table 1), and hence, the sample interval (Δt in Eq. (1)) is 10 s.

[1] The CPC minimum detectable diameters we report are in fact diameters that a CPC detects particles with efficiency = 50 %. The CPC detection efficiency is a steep function of particle diameter (Wiedensohler et al. 1997).

153 ## 3 Analysis

154 ### 3.1 Air Mass Classification and Air Parcel Trajectories

155 Locations close to the Arauco Site are shown in Fig. 1. A significant pollution source in
156 the region is the Arauco paper mill which releases 600 ton/yr of SO_2 (Arauco Woodpulp 2010).
157 When winds had an easterly component, the paper mill may have affected air quality at the
158 Arauco Site. Other pollution sources are Concepción (population 950,000), Coronel (population
159 110,000), Curanilahue (population 32,000), Lebu (population 24,000), and Cañete (population
160 32,000). In addition, many residences in the region, including the residence where we operated
161 the CPC and UHSAS, burn wood for residential heating.

162 In a subsequent section, we compare CPC data from the Arauco Site to values measured
163 at NOAA's Trinidad Head (THD) observatory in Northern California (41.05° N, 124.2° W, 107
164 m MSL). The THD dataset includes contamination from local sources (e.g., campfires lit by day
165 visitors at the Trinidad State Beach Picnic Ground). Additionally, Mckinleyville, CA (population
166 15,000) and Arcata, CA (population 18,000) are the two coastal population centers reasonably
167 close to THD. Both are southeast of the THD, at distances between 15 and 25 km. Northern
168 California's large population centers (San Francisco Bay Area and Sacramento) are ~ 300 km
169 southeast of the THD. An important distinction between the sampling at THD and Arauco is the
170 above ground level (a.g.l.) height of the aerosol inlets. This is 10 and 2 m a.g.l. at THD and
171 Arauco, respectively. We cannot state with any certainty if the lower-height sampling at Arauco
172 made those measurements unrepresentative.

173 Wind measurements made at the Arauco Site (Sect. 2.1) and the THD were used to
174 conditionally sample the CPC measurements. At Arauco, wind directions from 180° to 330°
175 were chosen as the clean sector. At THD, the clean sector was chosen from 210° to 360°. The

clean sectors at Arauco and THD are shown in Fig. 2. Three factors entered into our selection of the clean sectors: 1) Inclusion of winds from either true south (Arauco Site) or true north (THD), 2) the same range of angles (150^o) at both sites, and 3) exclusion of wind from the directions of regional population centers.

Additionally, we used HYSPLIT back trajectories (NOAA 2016) to conditionally sample Arauco Site aerosol measurements associated with onshore-moving air. The back trajectories were initialized at 00, 06, 12, and 18 UTC. In addition to these static arrival times, trajectories were calculated with the coordinates of the Arauco Site [2] and with wind fields from the Global Data Assimilation System. The spatial resolution of the wind data is 0.5^o. Position along a trajectory was evaluated hourly. Trajectories that were over the ocean continuously for three days before landfall, and had a direction within the clean sector one hour before arriving at Arauco, were classified as "onshore" trajectories. There are 20 onshore trajectories that overlap with the availability of CCOPE UHSAS measurements.

In subsequent sections, a set of 20 two-hour data segments, centered on the onshore trajectory arrival times, are further analyzed. Appendix B describes the numerical filter we used to derive the aerosol properties analyzed in Sect. 4.2, 4.3, 4.4, and 4.5. The filter attenuates aerosol property variability occurring on time scales shorter than 100 s. We developed the filter to remove narrow "spikes" in the concentration sequences (CPC and UHSAS) which seem to have originated from local sources of aerosol pollution. The Supplementary Material has plots of filtered aerosol properties corresponding to each of the 20 two-hour segments. Four of these were impacted aerosol variability at scales larger than 100 s. In general, these features were not

[2] Trajectory starting altitude was set at 60 m MSL (5 m above the Arauco site)

attenuated by the numerical filter. In these instances we discarded (subjectively) portions of the two-hour segment and retained a subset for the analyses conducted in Sect. 4.3, 4.4 and 4.5.

Trajectory altitude is important for determining the presence of SSA particles. Onshore trajectories originating from relatively close to the sea surface, and thus classified as onshore "sea surface" trajectories, were required to have pressures > 980 hPa over their three-day advection to the Arauco Site. Eighteen of the 20 onshore trajectories were also sea surface trajectories. An example of a sea surface trajectory is shown in Figs. 3a - b. The sea surface wind speed (U), analyzed in Sect. 4.5, is the average of the six hourly trajectory speeds in the six-hour window ending six hours before the trajectory arrived at the Arauco site. The averaging interval is shown in Fig. 3b. Two onshore trajectories, classified as "aloft", had pressures substantially smaller than 980 hPa over their three-day advection to the Arauco Site.

3.2 Sea Salt Aerosol

Correlated values of SSA concentration and sea surface wind speed are reported in many publications. In a review of the topic, Lewis and Schwartz (2004; hereafter LS04) used a particle's deliquesced wet size, evaluated at 80% relative humidity, to group SSA particles into three size classes. In field studies conducted at a coastal site, Clarke et al. (2003) demonstrated that particles sizing in the middle of LS04's small particle size class - those with a dry diameter larger than 0.5 μm or a RH = 80% wet diameter larger than 1 μm – had a composition that was dominated by sea salt (NaCl).

By restricting our focus to segments of the CCOPE data associated with sea surface trajectories (Sect. 3.1), we will analyze UHSAS measurements of particles with $D > 0.5$ μm ($N_{>0.5}$) and will assume that this subset of the ASD corresponds to SSA particles. This lower-limit size is a factor of two smaller than the RH = 80% diameter corresponding to the middle of

LS04's small SSA class. This is because we assumed that particle size decreased as the aerosol stream warmed from its ambient temperature to the temperature of the UHSAS measurement. Support for this assumption is provided in Appendix A.

3.3 Moments of the Aerosol Size Distribution

In our analysis, we calculated three moments of the UHSAS-measured ASDs. These are the aerosol concentration (N_{UHSAS}), aerosol surface area (S_{UHSAS}), and aerosol volume (V_{UHSAS}). We symbolize these moments as integrals (Eq. (2) – (4)).

$$N_{UHSAS} = \int (dN/dlog_{10}D)\cdot dlog_{10}D \quad (2)$$

$$S_{UHSAS} = \pi \int D^2 (dN/dlog_{10}D)\cdot dlog_{10}D \quad (3)$$

$$V_{UHSAS} = (\pi/6) \int D^3 (dN/dlog_{10}D)\cdot dlog_{10}D \quad (4)$$

In these formulae the group $(dN/dlog_{10}D)\cdot dlog_{10}D$ represents the concentration of aerosol particles with diameter between $log_{10}D$ and $log_{10}D + dlog_{10}D$. Hence, when plotted versus the logarithm of particle diameter, the area under the $dN/dlog_{10}D$ curve is proportional to the size-integrated concentration. This is demonstrated in Figs. 4a – b where the size-integrated concentration is ~ 300 cm^{-3} in onshore-moving air (Fig. 4a), and the concentration is approximately four times larger (~ 1100 cm^{-3}) in air thought to be contaminated by continental sources (Fig. 4b). Also apparent is the right-tail of an Aitken mode, at ~ 0.06 μm in Fig. 4a (onshore-moving air), the absence of an Aitken mode in Fig. 4b (continental air), at least at diameters detectable by the UHSAS (D > 0.055 μm; Table 1), and the presence of an accumulation mode at ~ 0.1 μm in both airmasses (Figs. 4a – b). Two aspects of these results, i.e. the absence of an Aitken mode plus the dominance of an accumulation mode, in polluted coastal air, is consistent with ASDs reported in Raes et al. (1997) and in Dall'Osto et al. (2009).

4 Results

4.1 Comparison of CPC data from the Arauco Site and the THD

In this section, CPC-measured concentrations from the Arauco Site and from NOAA's THD observatory are compared. At THD, CPC measurements were made using a TSI 3760 condensation particle counter. The minimum particle diameter detected by the TSI 3760 (D = 0.015 μm; Wiedensohler et al. 1997) is slightly larger than that in the TSI 3010 (D = 0.012 μm; Table 1). We ignored this distinction.

The THD dataset spans the years 2002 to 2014. Because CCOPE was a wintertime field study, only December, January, and February THD data are used in the comparison. There are 24,346 data points (hourly averaged) from THD and 5,541 classify as clean sector. In comparison, there are 745 data points from the Arauco Site (hourly averaged) and 194 classify as clean sector. For both sites, we required a clean sector wind speed > 1.5 m s^{-1} in addition to the clean sector directional criteria (Fig. 2). Because the numerical filter (Sect. 3.1) requires 1 Hz CPC measurements, and since 1 Hz measurements are unavailable in the THD data archive, the filter was not applied to either of the data sets analyzed in this section.

In the following paragraph we compare hourly-averaged CPC-measured concentrations from the Arauco Site and THD. Because the number of data points in these data sets is different, a particular statistical comparison methodology was applied. The approach followed here compares the Arauco and THD average concentrations by applying the Student's t-distribution method (t-test) explained in Havlicek and Crain (1988; their Eq. (10.6) and (10.7)). The statistical hypotheses are: A) Null hypothesis: averages are equal, and B) Alternate hypothesis: averages are different. We also applied the non-parametric Wilcoxon Rank-Sum Test (rs_test; Interactive Data Language, Harris Geospatial Solutions, Inc.). Statistical inference that we derive

265 based on the Wilcoxon Rank-Sum Test (not shown) is consistent with what we describe below
266 using the t-test.

267 Two aspects of the Arauco/THD comparison are presented here; more detail is available
268 in Fults (2016). First, clean sector measurements are compared. The mean N_{CPC} at Arauco is
269 2759 cm^{-3} (standard deviation σ = 1827 cm^{-3}). The mean and σ at THD are 858 ± 729 cm^{-3}. Fig. 5
270 shows the Arauco and THD N_{CPC} probability distribution functions. Of note is the larger mode
271 concentration and broader distribution at Arauco. Based on our t-test comparison, the Arauco
272 average is larger than the THD average ($p < 0.01$). Second, Arauco and THD concentrations are
273 compared without regard to wind direction. The average at the Arauco Site is 2971 cm^{-3} ± 1802
274 while at THD the average is 1059 cm^{-3} ± 855 cm^{-3}. These averages are also statistically different
275 ($p < 0.01$), and again, the Arauco average is larger than that at THD. Based on averages
276 presented in this section, and information provided in Table 2, two summary statements are
277 warranted: 1) During wintertime, the THD classifies as a moderately-polluted marine site,
278 and the Arauco Site classifies between moderately-polluted marine and heavily-polluted
279 marine. 2) These sites are not representative of conditions well removed from anthropogenic
280 influence.

281 **4.2 Continental Contamination**

282 In this section we probe why aerosol properties varied strongly during four of the 20
283 onshore trajectories. Among these, the example presented in Figs. 6a – c exhibits the largest
284 degree of CPC and UHSAS variability. During this two-hour data segment, centered on 00 UTC
285 June 9 (9 pm local time), winds were light at Arauco and Curanilahue (≤ 1 m s^{-1}) and the wind
286 direction was variable at Curanilahue (Arauco Site wind direction measurements are only
287 available after 19 June 2015; Sect. 2.1).

Over the ocean, 12 to 6 hours prior to 00 UTC June 9, the HYSPLIT wind speed was 8.3 m s^{-1} and the HYSPLIT direction was westerly (Fig. 3a). In terms of UHSAS measurements (Figs. 6a – c), an obvious feature is the variability in the sequences of N_{UHSAS}, V_{UHSAS}, and S_{UHSAS}. The S_{UHSAS} is largest during an enhancement at ~ 00:37 UTC. The question arises: Can winds over the ocean and the resultant SSA production cause this variability, or must continental aerosol sources be evoked to explain this? This was addressed by calculating aerosol surface areas as a function of wind speeds that bracket the HYSPLIT-derived wind speed (8.3 m s^{-1}). The basis for this calculation is the *S*-on-*U* parameterization described in LS04 (their Fig. 22). The calculation indicates that *S* can range between 6 μm^2 cm^{-3} (U = 6.3 m s^{-1}) and 15 μm^2 cm^{-3} (U = 10.3 m s^{-1}). Since the upper-limit of the predicted variation is small compared to S_{UHSAS} at ~ 00:37 UTC (Fig. 6c), and at other times in Fig. 6c, and because the wind speed variation applied in the calculation is an order of magnitude larger than the variation in the HYSPLIT-derived wind speed (± 0.1 m s^{-1}), it is concluded that the aerosol enhancements seen in Figs. 6a – c are not due to a wind speed increase over the ocean. Rather, we surmise that aerosols emitted by continental Chilean sources were sampled during portions of the segment in Fig. 6. Vertical dashed lines indicate the subset of the two-hour segment we picked (subjectively) as being representative of onshore-moving air that was not affected, or only moderately affected, by emissions from continental Chilean sources. However, we do not expect our conditional sampling (based on HYSPLIT) and subjective picking (e.g., Fig. 6) to select aerosol properties representative of pristine marine air. Rather, we view these strategies as way to isolate aerosol properties associated with onshore-moving air that was less affected by continental sources compared to the other portions of the CCOPE data set.

Portions of three other two-hour segments were also discriminated into a period of onshore-moving air that was less affected by continental aerosols compared to an adjacent portion (or portions) of the two-hour data segment. This is shown in the Supplementary Material. Only measurements seen plotted between the vertical dashed lines in the Supplementary Material are analyzed in Sect. 4.3, 4.4, and 4.5.

4.3 Using N/V ratios to Parameterize Cloud Droplet Concentration

In this section we analyze two ASD moments (Sect. 3.3). These are symbolized N_{UHSAS} and V_{UHSAS}, respectively. The ratio of N_{UHSAS} (aerosol concentration) and V_{UHSAS} (aerosol volume) – generically the *N/V* ratio - is of interest for several reasons. First, for both operational and theoretical reasons the *N*/*V* ratio is evaluated for particle diameters larger than ~ 0.1 μm (VD00; Hegg and Kaufman 1998, hereafter HK98), and importantly, the model developed to evaluate aerosol exchange between an overlying free troposphere (FT) and the marine boundary layer (MBL) successfully predicts the *N/V* ratio in the MBL (VD00). Second, a value of the ratio can be derived by fitting measurements of *N* and *V* (HK98). Third, aerosol mass loading, and thus an aerosol volume corresponding to an assumed particle density [3], are relatively easy to evaluate. A method routinely used to evaluate aerosol mass loading involves pulling aerosol-laden air through a filter and evaluating the accumulated mass gravimetrically. Fourth, the product of an *N*/*V* ratio and an ambient aerosol volume (aerosol mass) has been proposed as a scheme for estimating cloud droplet concentration in marine stratocumulus clouds (HK98 and VD00).

HK98 used a passive cavity aerosol spectrometer probe (PCASP) to evaluate *N*, *V* and the *N/V* ratio. Since the UHSAS counts down to a smaller diameter (0.055 μm) than the PCASP

[3] In the case of ambient particles containing hygroscopic materials, density values range between 1.5 and 1.8 g cm^{-3} (McMurry et al. 2002)

(0.12 μm), it is expected that the *N/V* ratios we derive using the UHSAS will be larger than those in HK98. The main reason for this is that decreasing the lower-limit diameter increases *N* more than *V* (VD00).

As in HK98, linear least-squares regression analysis with an equation of the form $Y = a \cdot X$ was used to derive *N/V* ratios. Values of N_{UHSAS} and V_{UHSAS} entered into the regressions were derived with the lower-limit diameter set at 0.055 μm (Table 3) and 0.12 μm (Table 4). The latter allows comparison to *N/V* ratios in HK98. Tables 3 and 4 show the ratios and the fact that all of the Pearson correlation coefficients (*r*) are positive. With the exception of trajectories arriving at 12 UTC June 5 and 06 UTC June 8 (Table 3), and at 00 UTC June 9 (Table 4), all of the *N/V* correlations are statistically significant at $p < 0.01$.

As expected, the average *N/V* ratio in the fifth column of Table 3 (417 ± 297 μm^{-3}) is larger than that in HK98 (223 ± 76 μm^{-3}). These averages are different at $p = 0.01$. Table 4 has results based on the larger lower-limit diameter (0.12 μm). In that comparison, the Arauco *N/V* ratio (159 ± 100 μm^{-3}) does not differ significantly from HK98's (i.e., $p > 0.01$).

Application of the *N/V* ratio to aerosol-cloud-precipitation modelling requires knowledge of the aerosol volume, or alternatively, knowledge of the aerosol mass loading and the aerosol particle density. The aerosol volume is then multiplied by an average *N/V* ratio (e.g., the average at the bottom of the fifth column of Table 4), and their product is taken to be the modelled cloud droplet concentration (HK98 and VD00). This is straight forward, at least from the perspective of incorporating an aerosol-induced cloud feedback into a simulation, but it suffers from requiring additional information about the aerosol (aerosol volume). Because the UHSAS was unavailable for much of CCOPE (Table 1), aerosol volume is also unavailable. Another drawback is the

implicit assumption that only aerosol particles larger than the lower-limit diameter (e.g., 0.12 μm in Table 4) form cloud droplets.

4.4 Using Size Distribution and N_{CPC} to Parameterize CCN Activation Spectra

Andreae (2009) analyzed a set of aerosol concentration measurements obtained from collocated CPC and CCN instruments. Andreae's CPC measurements represent the concentration of particles *no smaller than* a particular diameter (~ 0.01 μm; Sect. 2.2), and his CCN measurements represent the concentration of particles that activate cloud droplets at a water vapor supersaturation (*SS*) *no larger than* a particular value (Rogers and Yau, 1989; chapter 6). The latter is *SS* = 0.4 % in Andreae (2009).

Similar to the relationship between CCN concentration at *SS* = 0.4 % and CPC concentration (Andreae, 2009; his Fig. 2), we now describe how CPC and UHSAS data from CCOPE can be used to develop a function that describes CCN activation spectra. In the parameterization we develop, the independent variable is a CPC-measured aerosol concentration. While only estimates, the activation spectra we obtain represent an important step toward evaluating how CCN affected cloud and precipitation during CCOPE. We envision this assessment will be advanced when our activation spectra are used to initialize numerical models.

Our first step is to select a particle diameter, apply this as a lower-limit diameter in an integration of the UHSAS size distribution, and divide the integral by the coincident CPC-measured concentration. The resultant is referred to as the *fractional aerosol concentration* (*FAC*).

$$FAC(D) = \frac{1}{N_{CPC}} \cdot \int_{D}^{1\mu m} \left(dN / d\log_{10} D \right) \cdot d\log_{10} D \qquad (5)$$

Figs. 7a - b have graphical representations of *FAC*(*D*=0.055 μm) and *FAC*(*D*=0.120 μm).

In a second step we interpret a *FAC*'s lower-limit diameter as an upper-limit *SS*. We do this by applying a value for the kappa hygroscopicity parameter, which we set at $\kappa = 0.5$, and by applying the kappa–Köhler formula of Petters and Kreidenweis (2007, their Eq. (6)). This transformation from lower-limit *D* to upper-limit *SS* converts the *FAC* in Fig. 7a to *FAC*(*SS* = 0.41 %) and the FAC in Fig. 7b to *FAC*(*SS* = 0.13 %). We also evaluated how a range of the kappa parameter ($0.3 < \kappa < 0.7$) translates to a range of *SS*. Our upper-limit κ comes from airborne measurements made over the Southeast Pacific Ocean during summer (Snider et al., 2017), and our lower-limit κ is the value recommended by Andreae and Rosenfeld (2008) for simulating aerosol indirect effects over continents.

The *FAC*s in Figs. 7a – b are two of the many available from CCOPE. One way to aggregate these is to calculate a *FAC* for each of the 20 onshore trajectories. For example, if we select the lower-limit diameter at $D = 0.055$ μm, plot numerator values (Eq. (5)) vs denominator values (Eq. (5)), and fit with the equation $Y = a \cdot X$, the "*a*" we derive is the *FAC*($D = 0.055$ μm) for a particular trajectory. *FAC*s calculated in this way, and with lower-limit *D* selected = 0.120 μm, are presented in the seventh columns of Tables 3 and 4. Correlation coefficients presented in the eighth columns of these tables mostly exceed 0.5. By averaging over the 20 onshore trajectories, we calculated the overall averages presented at the bottom of the two tables. These overall averages are *FAC*($D = 0.055$ μm) = 0.35 ± 0.13 (Table 3) and *FAC*($D = 0.120$ μm) = 0.13 ± 0.07 (Table 4). This decrease of the *FAC* results because a larger lower-limit *D* (Eq. (5)), implies a smaller numerator (Eq. (5)), and thus a smaller *FAC*(*D*).

What we refer to as *ensemble-averaged FAC*s were derived by selecting from all 20 onshore trajectories the numerator- and denominator-values represented in Eq. (5). The selected data pairs were fitted in the manner discussed previously. In addition, upper and lower quartile

values of the fitted slopes were calculated by applying the technique of Wolfe and Snider (2012; their Fig. 4d). We evaluated four ensemble-averaged *FAC*s corresponding to four selected diameters (D = 0.070, 0.095, 0.120, and 0.200 μm). The *FAC* at D = 0.055 μm was eliminated from this analysis because Kupc et al. (2018) showed that UHSAS measurements, at $D \leq 0.070$ μm, are negatively biased. Results are presented as circles in Fig. 8 and vertical error bars represent the quartile range. Values plotted on the abscissa correspond to the four diameters, each transformed to an *SS* using the kappa–Köhler formula with $\kappa = 0.5$, and horizontal error bars extend from most hygroscopic ($\kappa = 0.7$), at the left-most limit, to least hygroscopic ($\kappa = 0.3$), at the right-most limit.

In Fig. 8 we used power laws of the form $FAC(SS) = C \cdot SS^k$ (i.e., the form commonly used to parameterize CCN activation spectra (Twomey 1959)) to fit the points. The change in the slope of the fit function, seen here at SS = 0.15%, seems consistent with analyses demonstrating that in polluted marine cloud conditions, albeit during summertime, the exponent "k" in the Twomey power fit function is ≥ 1 and ≤ 1 at $SS < 0.1$ % and $SS > 0.1$ %, respectively (Hudson and Nobel 2014; data from the MASE project in their Fig. 1).

Our parameterized CCN activation spectrum (Fig. 8) is relevant to cloud-aerosol-precipitation modeling for several reasons. First, some numerical models treat *SS* as a prognostic variable and thus require initialization with a CCN activation spectrum (e.g., Khairoutdinov and Kogan 2000). Similarly, some models initialize with a particle size-dependent ASD function and use Köhler theory to derive a model-initializing CCN activation spectrum (e.g., Lebo et al. 2012). As described in these two references, these models initialize with a nonspecific CCN activation spectrum. If those models were used to investigate wintertime clouds and precipitation on the Central Chilean Coast, our parameterization could be applied as a CCOPE-specific

initialization. Second, since we have measurements of N_{CPC} for the totality of CCOPE (Table 1), and we have shown how an ensemble-averaged CCN activation spectrum can be developed with N_{CPC} as the input parameter – i.e. as $N(SS) = FAC(SS) \cdot N_{\mathrm{CPC}}$ – our parameterization can be used to estimate activation spectra for the complete CCOPE campaign. Third, model initiation with a specific CCN activation spectrum, as opposed to initialization with a regime-dependent droplet concentration (e.g., Thompson et al. 2004), is justified by sensitivities to cloud droplet activation reported in several publications (Cooper et al. 1997; Hudson and Yum, 1997; Snider et al., 2017).

An assumption implicit in our development is that particles were internally mixed within each of the four particle size classes. This seems justified by our use of HYSPLIT to conditionally sample (Sect. 3.1), and by the fact that the sampled airmasses were resident in the marine boundary layer for hours to days while subject to a variety of processes (Brownian coagulation and reactive uptake of SO_2, among others) that produce aerosols consistent with the internal mixture assumption (Fierce et al. 2017). An aspect of our measurements also supports the internal mixture assumption. Fig. 7b shows that number concentration corresponding to the 0.120 to 1 μm class is dominated by particles with diameters at the lower end of that class. Hence, the contribution of freshly emitted SSA particles, generally thought to size at dry diameters larger than 0.5 μm (Clarke et al. 2003; LS04), and with a $\kappa = 1.2$ (Berg et al. 1998), is typically small. A different bias would result if particles with κ values smaller than the lower-limit value ($\kappa = 0.3$) contributed significantly to the size-integrated concentration in Eq. (5). Burning biomass is an important source for such low-hygroscopicity particles (Carrico et al. 2005). Our conditional sampling (Sect. 3.1), combined with our filtering of the CPC and UHSAS measurements (Sect. 3.1 and Appendix B), reduces this concern.

4.5 Regression of $N_{>0.5}$ and Sea Surface Wind Speed

As discussed in Sect. 3.2, $N_{>0.5}$ represents the concentration of particles larger than 0.5 μm. We now support our conjecture that particles grouped into the $N_{>0.5}$ subset are indeed SSA. We do this by analyzing the correlation between $N_{>0.5}$ and sea surface wind speed (U). Sect. 3.1 explains how we used HYSPLIT to derive U.

Values of $N_{>0.5}$, corresponding to the 18 sea surface trajectories (Sect. 3.1), are plotted against U in Fig. 9. Linear least-squares regression analysis with a model equation of form $\ln(N_{>0.5}) = \ln(N_o) + a_N \cdot U$ was used to derive the coefficients N_o and a_N (O'Dowd and Smith 1993; LS04). The fitted coefficients are $N_o = 0.15$ cm^{-3} and $a_N = 0.38$ and the derived function (black curve) is shown in Fig. 9. The dashed black curves represent the 95% confidence interval (Romano 1977; his Eq. (4.2.3.f)). Also plotted (pink line) is the function derived by O'Dowd and Smith (1993) for dried SSA particles with diameter between 0.38 and 0.84 μm. Given that the O'Dowd and Smith (1993) function (their Fig. 7a) is associated with statistical uncertainty comparable to what we estimate for our data set, we are only moderately confident that the function we derived is a consequence of wind-generated SSA. Two caveats require mentioning. First, a fraction of our data points (~ 25%) lie either above or below our confidence interval (Fig. 9). Meteorology can contribute to this variability, as when sea surface winds establish a SSA population, and the wind subsequently slacks, or speeds up, prior to advection onto the continent. This is expected because the atmospheric residence time of D ~ 0.5 μm particles, in the absence of precipitation, is several days (LS04, p. 76). Also, our unintentional sampling of particles generated over the continent is a concern. We have taken steps to eliminate those sources of contamination (Sect. 3.1 and Appendix B), but our methods are not foolproof.

5 Discussion

The measurements analyzed here are, to the best of our knowledge, the first to characterize aerosol microphysical properties on the Central Chilean Pacific coast during winter. Since the measurement site was relatively close to a population center (Arauco, Chile), and a SO_2 emitting paper mill, and because wood burning is an important source of residential heat in this region, we suspect that our measurements are influenced by these land sources. We mitigated against this by focusing on data collected during periods of onshore flow. Additional steps were taken to minimize contamination from land-based aerosol sources. These procedures are explained in Sect. 3.1, 4.2, Appendix B, and in the Supplementary Material.

A point of comparison is the summertime measurements reported in HK98. Their data were collected during airborne sampling over the western Atlantic in air that had advected from the United States. HK98's averaged aerosol surface area (131 ± 93 μm^2 cm^{-3}; their Table 2) is clearly larger than that for our 20 onshore trajectories (42 ± 27 μm^2 cm^{-3}; results not shown). However, a more relevant comparator would be low altitude measurements made off the Central Chilean Pacific during winter. As far as we know, the desired data set is not available. Values of aerosol surface area in the FT over the North and South Pacific are generally < 10 μm^2 cm^{-3} (Clarke 1992), suggesting that even during onshore flow the Arauco Site is affected by anthropogenic sources. We have assumed these sources are Chilean, however, a contribution from long range transport cannot be ruled out.

The larger winter-averaged CPC concentration at Arauco, compared to THD, is evidence for stronger continental contamination at the former. Since N_{CPC} is a parameter in our parameterization of CCN activation spectra (Sect. 4.4), we conclude that cloud droplet concentrations in low level marine clouds (stratocumulus) formed in the vicinity of Arauco are

larger than in similar clouds near THD. If true, this conclusion would be opposite the general situation in Southern Pacific boundary layer clouds where cloud droplet concentrations are statistically less than in their Northern hemispheric counterparts (Bennartz 2007). Relevant to this, Bennartz (2007) comments on a coast-normal droplet concentration gradient that is stronger on the Central Chilean coast compared to the California/Oregon coast. We presume that the gradient exists because of the larger concentration of aerosols over continents (Andreae and Rosenfeld, 2008), and because of aerosol removal that occurs within and below marine stratocumulus clouds. In addition, Bennartz (2007) demonstrates that the coast-normal droplet concentration gradient is larger off the Central Chilean coast, compared to California/Oregon coast, in part because oceanic concentrations, ~ 2000 km offshore, are generally smaller in the south compared to the north Pacific. Whether the southern hemispheric gradient is also enhanced by larger aerosol concentrations over coastal Central Chile, compared to coastal California and Oregon, is an open question. Further analysis of the satellite retrievals analyzed by Bennartz (2007), with segregation into wintertime and summertime categories, as well as measurements conducted at an offshore island location, or acquired using aircraft or ships, are needed to address this question.

6 Conclusions

Analyses presented here are based on Condensation Particle Counter (CPC) measurements made during one winter season (June, July and August 2015) on the Central Chilean Pacific coast (38 ^{o} S). Also analyzed are aerosol size distribution measurements made with an Ultra High Sensitivity Aerosol Spectrometer (UHSAS). UHSAS measurements are available from 29 May to 28 June (Table 1). Limitations of this study are proximity of the measurement site to a population center (Arauco, Chile) and a SO_2 emitting paper mill, sampling of particles emitted from residences close to where our instruments were operated, and the incomplete drying of the sampled aerosol particles. This first attempt to make CPC and ASD measurements on the Central Chilean Pacific coast during winter was exploratory and our results should be considered preliminary.

We compared CPC-measured concentrations from the Arauco Site to values acquired at the NOAA observatory Trinidad Head (THD) on the North Pacific Coast of California. The averaged CPC concentration is larger at the Arauco Site and that difference is evident in an Arauco/THD comparison based on air arriving from all wind directions and from clean sector directions. In addition, we conditionally sampled UHSAS-measured size distributions and derived parameterized descriptions of sea salt aerosol (SSA) and cloud condensation nuclei (CCN) for periods of onshore flow. In these parameterizations the input parameters are respectively sea surface wind speed and CPC-measured concentration.

In the context of CCOPE, there are two precipitation regimes that impact the Central Chilean Coast and the Nahuelbuta Mountains during winter (Massmann et al. 2017). The first of these have radar-derived echo tops at ~ 2 km MSL and produce rain by direct conversion of cloud droplets to rain drops. The second have higher echo tops, extending to temperatures colder

than 0 ^{o}C and produce rain that is, at least in part, initiated by ice phase processes. Investigation of the rain produced in the shallow regimes is an active area research; it is thought that SSA and the CCN play important roles (Feingold et al. 1999; Gerber and Frick 2012). The deep regimes form precipitating hydrometeors (ice particles) at cloud temperatures < 0 ^{o}C. Again, aerosols play a role, but there are many facets to this and first-order effects are not yet agreed on. Perhaps foremost is the role played by aerosol acting as ice nuclei. Measurement of an ice nuclei activation spectrum, development of an ice particle parameterization, and incorporation of the parameterization into a numerical model are needed to explore this dimension of the problem. Because they modulate cloud droplet size, the development of graupel, and influence latent heating (e.g., Tao et al. 2012), the CCN and SSA likely also play a role in the deep regimes. Thus, we anticipate that modeling of both precipitation regimes will benefit from the CCN and SSA parameterizations presented here.

Author Contribution

Jeff Snider, Jason Minder, David Kingsmill wrote successful proposals that funded this research. Sara Fults, Adam Massman, Aldo Montecinos, and David Kingsmill performed the field measurements. Rene´ Garreaud and Aldo Montecinos provided logistical support during the field phase of the project. Elisabeth Andrews provided data from THD. Sara Fults wrote her MS dissertation and this was adapted to this manuscript by Jeff Snider. All authors contributed to the editing of this manuscript.

Acknowledgments

We thank Freddy Echeverría-Cabezas for his assistance during CCOPE, Matthew Burkhart for building the aerosol data acquisition system, Zhien Wang for providing a graduate assistantship, Nicholas Mahon for shipping logistics, and the Departamento de Geofísica at the Universidad de Concepción. This work was supported by the United States National Science Foundation Physical and Dynamic Meteorology Division under Awards AGS-1522277 and AGS-1522939.

Data Availability

CCOPE CPC and UHSAS data, and a data reader (Interactive Data Language, Harris Geospatial Solutions, Inc.), are at http://www-das.uwyo.edu/~jsnider/CCOPE/.

Appendix A

Because the *RH* at the Arauco Site was often in excess of 80 % (Fig. A1c), particles entering the sample tube (Sect. 2.2) were haze droplets (Rogers and Yau 1989). As these haze droplets transit the sample tube they experience an increase in temperature, an *RH* decrease, and thus a decreased *D*. The lowest *RH* experienced by a haze droplet is at the point of detection where the aerosol temperature is presumed to be the internal "box temperature" measured by the UHSAS. The *RH* at this point is

$$RH_U = \frac{RH_A \cdot e_s(T_A)}{e_s(T_U)} \quad \text{(A1)}$$

where T_U is the internal UHSAS temperature, e_s is saturation vapor pressure (temperature dependent), and RH_A and T_A are the ambient *RH* and temperature, respectively. In nearly all of the UHSAS sampling during CCOPE, the RH_U was less than 60 % (Fig. A1d). This suggests that the haze droplets detected by the UHSAS were partially dried. Partial drying of the haze droplets is supported by calculations (Lewis and Schwartz 2004; their Fig. 8) showing that a D = 4 μm NaCl haze droplet reaches its equilibrium size (D = 2 μm) in 0.1 s subsequent to a step-change of *RH* from 98 % to 80 %. Because 0.1 s is small relative to the average residence time of haze droplets within the sample tube (0.8 s), we ignored the possibility of a kinetic limitation to drying and we assumed that the haze droplets relaxed to their equilibrium size at RH_U prior to the time they were detected. Since we do not know the chemical composition of the haze droplets, their equilibrium size is uncertain, but calculations corresponding to RH_U = 60% and a haze droplet composed of sodium sulfate indicate that the equilibrium size is 30% larger than the corresponding dry particle size (Snider et al. 2017; their Fig. A2b). Three factors interact to partially compensate for a size overestimate due to incomplete particle drying: 1) Particle sizing

582 performed by the UHSAS was calibrated using polystyrene latex particles (refractive index n =
583 1.57 at λ = 1.05 μm (Marx and Mulholland 1983)); 2) Liquid water (n = 1.32 at λ = 1.05 μm
584 (Irvine and Pollack, 1968)) makes a significant contribution to the mass of a haze droplet at RH =
585 60% (here again we are assuming the above-mentioned sodium sulfate composition for the
586 completely dried particle); and 3) Assuming the same scattering intensity, an n = 1.6 particle
587 sizes 10% smaller than an n = 1.4 particle (Cai et al., 2008; their Fig. 1). Accepting the 10% as
588 an underestimate, and the above-mentioned 30% as an overestimate, we conclude that particle
589 sizes reported by the UHSAS were overestimated by 20%. We did not correct for this sizing bias.

590 Laboratory testing of the UHSAS and CPC is documented in Figs. A2a – b, and in Figs.
591 A3a - b. We evaluated consistency among measurements made with the UHSAS, the CPC, and a
592 Scanning Mobility Particle Scanner (SMPS; TSI 2000b). In all of these tests, the RH of the test
593 aerosols was < 15 %. An example ASD derived using the UHSAS (pink) and the SMPS (black)
594 is shown in Fig. A2a. In this test the three instruments (UHSAS, CPC and SMPS) were sampling
595 mobility-selected ammonium sulfate particles with D = 0.075 μm. The refractive index of this
596 material at λ = 1.05 μm is n = 1.51 (Toon et al., 1976). It is evident that the mode diameter
597 measured by the UHSAS is smaller than that reported by the SMPS (D = 0.075 μm). This
598 difference is qualitatively consistent with the smaller refractive index of the test material
599 (ammonium sulfate), compared to the larger refractive index of the polystyrene latex particles
600 used by the factory to calibrate the UHSAS (DMT, 2013). Fig. A2b shows a test with D = 0.71
601 μm polystyrene latex particles. As expected, the mode diameter in the UHSAS size distribution
602 is in agreement with the mode size in the SMPS size distribution.

603 An additional feature of our laboratory testing is the multi-modal structure in the SMPS
604 size distribution at D < 0.5 μm (Fig A2b). This structure results because the particle diameter

605 inferred by the SMPS depends on the physical diameter of the test particles, and on also depends
606 on the test particle's charge state. The multi-modal structure at $D < 0.5$ μm corresponds to
607 particles carrying 5, 4, 3, and 2 fundamental charges, but each with physical diameter equal 0.71
608 μm. As stated in the previous paragraph, the latter is the diameter of the polystyrene test
609 particles.

610 Figs. A3a - b summarize all of the lab testing we conducted in support of CCOPE. In Fig.
611 A3a, N_{UHSAS} is plotted vs N_{CPC} for tests with $D < 0.2$ μm and Fig. A3b has tests with $D > 0.2$ μm.
612 On average, concentrations differ by ± 6 % in Fig. A3a ($D < 0.2$ μm) and by ± 10 % in Fig. A3b
613 ($D > 0.2$ μm).
614

Appendix B

For each of the onshore trajectories (Sect. 3.1), a two-hour segment, centered on the trajectory arrival time was analyzed. An example is in Figs. B1a – e. The first panel (Fig. B1a) shows the sequence of CPC values sampled every second (i.e., 1-s samples referred to as *fast* N_{CPC}), and Fig. B1b shows CPC values sampled every 10 seconds (i.e., 10-s samples referred to as *slow* N_{CPC}). The following procedure was used to attenuate the narrow perturbations that were likely the result of local aerosol emissions (e.g., within the time interval indicated by vertical dashed lines in Figs. B1a, B1b, and B1d).

First, the fast N_{CPC} values were used to determine, for each 10 s of the sequence, a concentration relative standard deviation (σ / <x>). Second, if the relative standard deviation was greater than 0.02 both the slow N_{CPC} measurement (sampled once every 10 second) and the ASD measurement (also sampled once every 10 second; Table 1) were discarded. Fig. B1c and Fig. B1e show the N_{CPC} and N_{UHSAS} sequences after application of the filter. These two filtered sequences (N_{CPC}(filtered) and N_{UHSAS}(filtered)), and the filtered values of aerosol surface area (S_{UHSAS}), aerosol volume (V_{UHSAS}), and D > 0.5 μm concentration ($N_{>0.5}$) are the focus of the bulk of our analysis.

References

Albrecht, B. A., Aerosols, cloud microphysics, and fractional cloudiness, Science, 245, 1227 – 1230, 1989

Andreae, M.O., Correlation between cloud condensation nuclei concentration and aerosol optical thickness in remote and polluted regions, Atmos. Chem. Phys, 9, 543-556, 2009

Andreae, M.O. and D. Rosenfeld, Aerosol-cloud-precipitation interactions. Part 1. The nature and sources of cloud-active aerosols, Earth-Sci. Rev., 89, 13 – 41, 2008

Arauco Woodpulp, accessed 16 December 2018 at: http://web.arauco.cl/_file/file_3382_pulp%20catalog.pdf, 2010

Bennartz, R., Global assessment of marine boundary layer cloud droplet number concentration from satellite, J. Geophys. Res., 112, D02201, 2007

Berg, O. H., E. Swietlicki, and R. Krejci, Hygroscopic growth of aerosol particles in the marine boundary layer over the Pacific and Southern Oceans during the First Aerosol Characterization Experiment (ACE 1), J. Geophys. Res., 103, 16535-16545, 1998

Birmili, W., A. Wiedensohler, J. Heintzenberg, and K. Lehmann, Atmospheric particle number size distribution in central Europe: Statistical relations to air masses and meteorology, J. Geophys, Res. Atmos., 106, 32005–32018, 2001

Boucher, O., and Coauthors, Clouds and Aerosols. In: Climate Change 2013: The Physical Science Basis. Contribution of Working Group I to the Fifth Assessment Report of the Intergovernmental Panel on Climate Change [Stocker, T.F., D. Qin, G.-K. Plattner, M. Tignor, S.K. Allen, J. Boschung, A. Nauels, Y. Xia, V. Bex and P.M. Midgley (eds.)], Cambridge University Press, Cambridge, United Kingdom, 2013

Brechtel, F. J., S. M. Kreidenweis, and H. B. Swan, Air mass characteristics, aerosol particle number concentrations, and number size distributions at Macquarie Island during the First Aerosol Characterization Experiment (ACE 1), J. Geophys. Res. Atmos., 103, 16351–16367, 1998

Cai, Y., J.R. Snider and P. Wechsler, Calibration of the passive cavity aerosol spectrometer probe for airborne determination of the size distribution, Atmos. Meas. Tech., 6, 2349-2358, 2013

Cai, Y., D.C.Montague, W.Mooiweer-Bryan and T.Deshler, Performance characteristics of the ultra high sensitivity aerosol spectrometer for particles between 55 and 800 nm: Laboratory and field Studies, J.Aerosol Sci., 39, 759-769, 2008

675 Carrico, C.M., S.M.Kreidenweis, W.C.Malm, D.E.Day, T.Lee, J.Carrillo, G.R.McMeeking, J.L.
676 Collett, Hygroscopic growth behavior of a carbon-dominated aerosol in Yosemite
677 National Park, Atmos. Environ., 39, 1393-1404, 2005
678
679 Clarke, A., Atmospheric Nuclei in the Remote Free-Troposphere, J. Atmos. Chem., 14, 479-488,
680 1992
681 Clarke, A., V. Kapustin, S. Howell, K. Moore, B. Lienert, S. Masonis, T. Anderson, and D.
682 Covert, Sea-salt size distribution from breaking waves: Implications for marine aerosol
683 production and optical extinction measurements during SEAS, J. Atmos. Ocean.
684 Technol., 20, 1362–1374, 2003
685
686 Cooper, W.A., R.T. Bruintjes, and G.K. Mather, Calculations pertaining to hygroscopic seeding
687 with flares, J. Appl. Meteor., 36, 1449 – 1469, 1997
688
689 Covert, D. S., V. N. Kapustin, P. K. Quinn, and T. S. Bates, New particle formation in the
690 marine boundary layer, J. Geophys. Res., 97(D18), 20581–20589,
691 doi:10.1029/92JD02074, 1992
692
693 Dall'Osto, M., and Coauthors, Aerosol properties associated with air masses arriving into the
694 North East Atlantic during the 2008 Mace Head EUCAARI intensive observing period:
695 an overview, Atmos. Chem. Phys. Discuss., 9, 26265–26328, 2009
696
697 Diesch, J. M., F. Drewnick, S. R. Zorn, S. L. Von Der Weiden-Reinmüller, M. Martinez, and S.
698 Borrmann, Variability of aerosol, gaseous pollutants and meteorological characteristics
699 associated with changes in air mass origin at the SW Atlantic coast of Iberia, Atmos.
700 Chem. Phys, 12, 3761-3782, 2012
701
702 DMT, Ultra High Sensitivity Aerosol Spectrometer (UHSAS) Operator Manual, Boulder, CO,
703 2013
704
705 Feingold, G., W. R. Cotton, S. M. Kreidenweis, J. T. Davis, and J. A. T. D. Avis, The Impact of
706 Giant Cloud Condensation Nuclei on Drizzle Formation in Stratocumulus: Implications
707 for Cloud Radiative Properties, J. Atmos. Sci., 56, 4100–4117, 1999
708
709 Fierce, L., N. Riemer, and T.C. Bond, Toward Reduced Representation of Mixing State for
710 Simulating Aerosol Effects on Climate. Bull. Amer. Meteor. Soc., 98, 971–980,
711 https://doi.org/10.1175/BAMS-D-16-0028.1, 2017
712
713 Fults, S., Aerosol measurements during the Central Chilean Orographic Precipitation
714 Experiment, M.S. Thesis, Department of Atmospheric Science, University of Wyoming,
715 2016
716
717 Garreaud, R., M.Falvey, and A.Montecinos, Orographic precipitation in coastal southern Chile:
718 Mean distribution, temporal variability, and linear contribution, J. Hydrometeor., 1185 –
719 1202, 2016
720

721 Gerber, H. and G.Frick, Drizzle rates and large sea-salt nuclei in small cumulus, J. Geophys.
722 Res., 117, D01205, 2012
723
724 Gras, J.L., Baseline atmospheric condensation nuclei at Cape Grim 1977-1987, J. Atmos. Chem.,
725 11, 89-106, 1990
726
727 Gras, J. L., CN, CCN and particle size in Southern Ocean air at Cape Grim, J. Atmos. Res.,
728 35, 233–251, 1995
729
730 Hansen, J., The Faustian Bargain: Humanity's Own Trap, Storms of My Grandchildren,
731 Bloomsbury, 320 pp., 2009
732
733 Havlicek, L.L., and R.D. Crain, Practical Statistics for the Physical Sciences, American
734 Chemical Society, 512 pp., 1988
735
736 Hegg, D. A., and Y. J. Kaufman, Measurements of the relationship between submicron aerosol
737 number and volume concentration, J. Geophys. Res., 103, 5671-5678, 1998
738
739 Hinds, W. C., Aerosol Technology: Properties, Behavior and Measurement of Airborne
740 Particles, John Wiley & Sons, INC, 483, 1999
741
742 Hoppel, W. a., G. M. Frick, J. W. Fitzgerald, and R. E. Larson, Marine boundary layer
743 measurements of new particle formation and the effects nonprecipitating clouds have, J.
744 Geophys. Res., 99, 14443–14459, 1994
745
746 Hudson, J.G. and S. Yum, Droplet spectral broadening in marine stratus. J. Atmos. Sci., 54,
747 2642–2654, 1997
748
749 Hudson, J.G., and S.Nobel, CCN and vertical velocity influences on droplet concentrations and
750 supersaturations in clean and polluted stratus clouds, J. Atmos. Sci., 312-331, 2014
751
752 Hudson, J.G., S.Noble, and S.Tabor, Cloud supersaturations from CCN spectra Hoppel minima,
753 J. Geophys. Res. Atmos., 120, 3436–3452, doi:10.1002/2014JD022669, 2015
754
755 International Civil Aviation Organization (ICAO), Manual of the ICAO Standard Atmosphere:
756 extended to 80 kilometres (262 500 feet), 3rd ed., ISBN-92-9194-004-6, 1993
757
758 Irvine, W.M. and J.B. Pollack, Infrared optical properties of water and ice spheres, Icarus, 8, 324
759 – 360, 1968
760
761 Khairoutdinov, M. and Y. Kogan, A new cloud physics parameterization in a large-eddy
762 simulation model of marine stratocumulus, Mon. Wea. Rev., 128, 229 - 243, 2000
763
764 Kupc, A., Williamson, C., Wagner, N. L., Richardson, M., and Brock, C. A.: Modification,
765 calibration, and performance of the Ultra-High Sensitivity Aerosol Spectrometer for
766 particle size distribution and volatility measurements during the Atmospheric

Tomography Mission (ATom) airborne campaign, Atmos. Meas. Tech., 11, 369-383, https://doi.org/10.5194/amt-11-369-2018, 2018

Lebo, Z. J., Morrison, H., and Seinfeld, J. H., Are simulated aerosol-induced effects on deep convective clouds strongly dependent on saturation adjustment?, Atmos. Chem. Phys., 12, 9941-9964, 2012

Lewis, E. R., and S. E. Schwartz, Sea Salt Aerosol Production: Mechanisms, Methods, Measurements, and Models, American Geophysical Union, 413 pp., 2004

Marx, E. and G.W. Mulholland, Size and refractive index determination of single polystyrene spheres, Journal of Research of the National Bureau of Standards, 88, 321 – 338, 1983

Massmann, A.K., J.R. Minder, R.D. Garreaud, D.E. Kingsmill, R.A. Valenzuela, A. Montecinos, S.L. Fults, and J.R. Snider, 2017, The Chilean Coastal Orographic Precipitation Experiment: Observing the Influence of Microphysical Rain Regimes on Coastal Orographic Precipitation. J. Hydrometeor., 18, 2723–2743, https://doi.org/10.1175/JHM-D-17-0005.1, 2017

McMurry, P.H., X.Wang, K.Park, and K.Ehara, The relationship between mass and mobility for atmospheric particles: A new Technique for measuring particle density, Aerosol Sci. Technol., 36, 227–238, 2002

McCoy, D.T., D.L. Hartmann, and D.P. Grosvenor, Observed Southern Ocean Cloud Properties and Shortwave Reflection. Part I: Calculation of SW Flux from Observed Cloud Properties. J. Climate, 27, 8836–8857, https://doi.org/10.1175/JCLI-D-14-00287.1, 2014

NOAA, HYSPLIT Trajectory Model, NOAA Air Resources Laboratory, Silver Spring, MD, Accessed 1 August 2016, [Available online at https://ready.arl.noaa.gov/HYSPLIT.php], 2016

O'Dowd, C.D., and M.H. Smith, Physicochemical properties of aerosols over the Northeast Atlantic: evidence for wind-speed-related submicron sea-salt aerosol production, J.Geophys. Res., 98, 1137-1149, 1993

Petters, M. D., J. R. Snider, B. Stevens, G. Vali, I. Faloona, and L. M. Russell, Accumulation mode aerosol, pockets of open cells, and particle nucleation in the remote subtropical Pacific marine boundary layer, J. Geophys. Res. Atmos., 111, 1–15, 2006

Petters, M. D., and S. M. Kreidenweis, A single parameter representation of hygroscopic growth and cloud condensation nucleus activity. Atmos. Chem. Phys., 7, 1961–1971, 2007

Raes, F., R. Van Dingenen, E. Cuevas, P. F. J. Van Velthoven, and J. M. Prospero, Observations of aerosols in the free troposphere and marine boundary layer of the subtropical Northeast Atlantic: Discussion of processes determining their size distribution, J. Geophys. Res., 102, 21315, 1997

Rogers, R. R., and M. K. Yau, A Short Course in Cloud Physics. 3rd ed. Permagon Press, 304 pp., 1989

Romano, A., Applied Statistics for Science and Industry, Allyn and Bacon Inc., pp. 385, 1977

Schwartz, S.E., Are global cloud albedo and climate controlled by marine phytoplankton?, Nature, 336, 441-445, 1988

Snider, J.R., D.Leon and Z.Wang, Droplet Concentration and Spectral Broadening in Southeast Pacific Stratocumulus, J. Atmos. Sci., 74, 719-749, 2017

Tao, W.-K., J.-P. Chen, Z. Li, C. Wang, and C. Zhang, Impact of aerosols on convective clouds and precipitation, Rev. Geophys., RG2001, 2012

Thompson, G., R.M. Rasmussen and K. Manning, Explicit forecasts of winter precipitation using an improved bulk microphysics scheme. Part I: Description and sensitivity analysis, Mon. Weather Rev., 132, 519 – 542, 2004

Toon, O.B., The optical constants of several atmospheric aerosol species: Ammonium sulfate, aluminum oxide, and sodium chloride, J. Geophys. Res., 81, 5733 - 5748, 1976

TSI, Inc., Condensation Particle Counter Instruction Manual, St. Paul, Minnesota, 2000a

TSI, Inc., Model 3080 Electrostatic Classifier Instruction Manual, St. Paul, Minnesota, 2000b

Twomey, S., Pollution and the Planetary Albedo, Atmospheric Environment, 8, 1251–56, 1974

Twomey, S., The nuclei of natural cloud formation part II: The supersaturation in natural clouds and the variation of cloud droplet concentration, Geofis. Pura Appl., 43, 243-249, 1959

van Dingenen, R., A. O. Virkkula, F. Raes, T. S. Bates, A. Wiedensohler, A simple non linear analytical relationship between aerosol accumulation number and sub-micron volume, explaining their observed ratio in the clean and polluted marine boundary layer, Tellus, 52B, 439-451, 2000

A. Wiedensohler, D. Orsini , D. S. Covert , D. Coffmann , W. Cantrell , M.Havlicek , F. J. Brechtel , L. M. Russell , R. J. Weber , J. Gras , J. G. Hudson & M. Litchy, Intercomparison Study of the Size-Dependent Counting Efficiency of 26 Condensation Particle Counters, Aerosol Science and Technology, 27:2, 224-242, DOI: 10.1080/02786829708965469, 1997

Wolfe, J. P., and J. R. Snider, 2012: A relationship between reflectivity and snow rate for a high-altitude S-band radar, J. Appl. Meteor. Climatol., 51, 1111–1128, 2012

858 Yum, S. S., and J. G. Hudson, Wintertime/summertime contrasts of cloud condensation nuclei
859 and cloud microphysics over the Southern Ocean, J. Geophys. Res., 109, 1-14, 2004
860

861 Table 1. Aerosol Instruments

Instrument and Reference	Aerosol Property Measured	Particle Diameter Range, μm	Aerosol Flow Rate, $cm^3\ s^{-1}$	Data Acquisition Rate, Hz	Data Availability (2015)
CPC Model 3010 (TSI 2000a)	Aerosol Concentration	$D > 0.012$	17	1	29 May to 14 Aug
UHSAS (DMT 2013)	Aerosol Size Distribution	$0.055 < D < 1$	0.34	0.1	29 May to 28 June

862

863

Table 2. Classification of Air Mass Type

Citation and Location	Measurement Site Characteristics	Air Mass Classification	Averaged CPC Concentration, cm^{-3} [a]
Gras (1990) Cape Grim, Tasmania 40.68 °S; 144.7 °E	Oceanic Wintertime	Remote Marine	100
Brechtel et al. (1998) Macquarie Island (Southwest Pacific) 54.50 °S; 159.0 °E	Oceanic Summertime	Remote Marine	700
Diesch et al. (2012) Portugal 37.11 °N; 7.735 °W	Coastal Continental Late Autumn	Moderately-polluted Marine Heavily-polluted Marine Continental	1000 7000 10000
This Study Arauco, Chile 37.25 °S; 73.34 °W	Coastal Continental Wintertime	Between moderately-polluted Marine and Heavily-polluted Marine	3000
This Study Trinidad Head, CA 41.05 °N; 124.2 °W	Coastal Continental Wintertime	Moderately-polluted Marine	1000

[a] Values rounded to one significant digit

Table 3. Statistics for Onshore Trajectories (D integration in Eq. (2), (4), and (5) is from 0.055 to 1 μm)

Arrival Hour, UTC	Type	Start DDHHMM [a], UTC	End DDHHMM [a], UTC	N_{UHSAS} on V_{UHSAS} Slope, μm^{-3}	r [b]	$FAC(D=0.055\ \mu m)$	r	Number of Samples
06	Sea Surface	050500	050700	93.	0.54	0.59	0.65	139
12	Sea Surface	051100	051134	64.	0.10	0.19	0.59	63
18	Sea Surface	051700	051900	110.	0.66	0.41	0.63	342
00	Sea Surface	052300	060100	298.	0.81	0.51	0.96	316
06	Sea Surface	060500	060700	60.	0.53	0.18	0.89	677
12	Sea Surface	061100	061300	91.	0.60	0.16	0.65	647
18	Sea Surface	061700	061900	107.	0.33	0.18	0.81	476
00	Sea Surface	062300	062325	234.	0.81	0.36	0.97	133
06	Sea Surface	080500	080700 [c]	163.	0.06	0.29	0.52	542
12	Sea Surface	081100	081300	358.	0.75	0.28	0.76	504
18	Sea Surface	081700	081900	450.	0.88	0.42	0.90	416
00	Sea Surface	090020	090033	764.	0.45	0.34	0.98	72
06	Sea Surface	090500	090700	703.	0.68	0.23	0.96	554
12	Sea Surface	091100	091300	714.	0.89	0.44	0.94	532
18	Sea Surface	091700	091900	675.	0.78	0.39	0.53	592
00	Sea Surface	092300	100100	519.	0.37	0.22	0.68	618
06	Aloft	100500	100700	857.	0.96	0.39	0.82	617
18	Sea Surface	101700	101900	825.	0.86	0.37	0.19	622
00	Sea Surface	110006	110031	834.	0.96	0.50	0.99	61
00	Aloft	262300	270100	420.	0.68	0.47	0.93	647
			<x>	417		0.35		
			σ	297		0.13		
			σ / <x>	0.71		0.36		

[a] DDHHMM indicates the start and end times (day in June 2015, hour, minute) of the data segment

[b] Pearson product moment for the $N_{UHSAS}(D=0.055\ \mu m)$ on $V_{UHSAS}(D=0.055\ \mu m)$ correlation

[c] Data recording ended at DDHHMM = 080646, i.e., 14 min before the stated end time

874 Table 4. Statistics for Onshore Trajectories (D integration in Eq. (2), (4), and (5) is from 0.120 to 1 μm)

Arrival Hour, UTC	Type	Start DDHHMM [a], UTC	End DDHHMM [a], UTC	N_{UHSAS} on V_{UHSAS} Slope, μm^{-3}	r [b]	$FAC(D$=0.120 μm)	r	Number of Samples
06	Sea Surface	050500	050700	60.	0.74	0.37	0.47	139
12	Sea Surface	051100	051134	40.	0.31	0.12	0.36	63
18	Sea Surface	051700	051900	64.	0.76	0.23	0.49	342
00	Sea Surface	052300	060100	113.	0.84	0.17	0.84	316
06	Sea Surface	060500	060700	34.	0.67	0.10	0.78	677
12	Sea Surface	061100	061300	44.	0.77	0.07	0.42	647
18	Sea Surface	061700	061900	42.	0.61	0.06	0.24	476
00	Sea Surface	062300	062325	107.	0.93	0.15	0.92	133
06	Sea Surface	080500	080700 [c]	89.	0.72	0.12	0.02	542
12	Sea Surface	081100	081300	139.	0.79	0.09	0.53	504
18	Sea Surface	081700	081900	202.	0.92	0.17	0.83	416
00	Sea Surface	090020	090033	184.	0.12	0.06	0.78	72
06	Sea Surface	090500	090700	228.	0.58	0.06	0.87	554
12	Sea Surface	091100	091300	262.	0.92	0.14	0.73	532
18	Sea Surface	091700	091900	257.	0.89	0.12	0.41	592
00	Sea Surface	092300	100100	204.	0.83	0.06	0.32	618
06	Aloft	100500	100700	323.	0.96	0.11	0.82	617
18	Sea Surface	101700	101900	279.	0.91	0.10	0.08	622
00	Sea Surface	110006	110031	346.	0.97	0.16	0.96	61
00	Aloft	262300	270100	171.	0.65	0.18	0.88	647
			<x>	159		0.13		
			σ	100		0.07		
			σ / <x>	0.63		0.55		

875

876 [a] DDHHMM indicates the start and end times (day in June 2015, hour, minute) of the data segment

877 [b] Pearson product moment for the $N_{UHSAS}(D$=0.120 μm) on $V_{UHSAS}(D$=0.120 μm) correlation

878 [c] Data recording ended at DDHHMM = 080646, i.e., 14 min before the stated end time

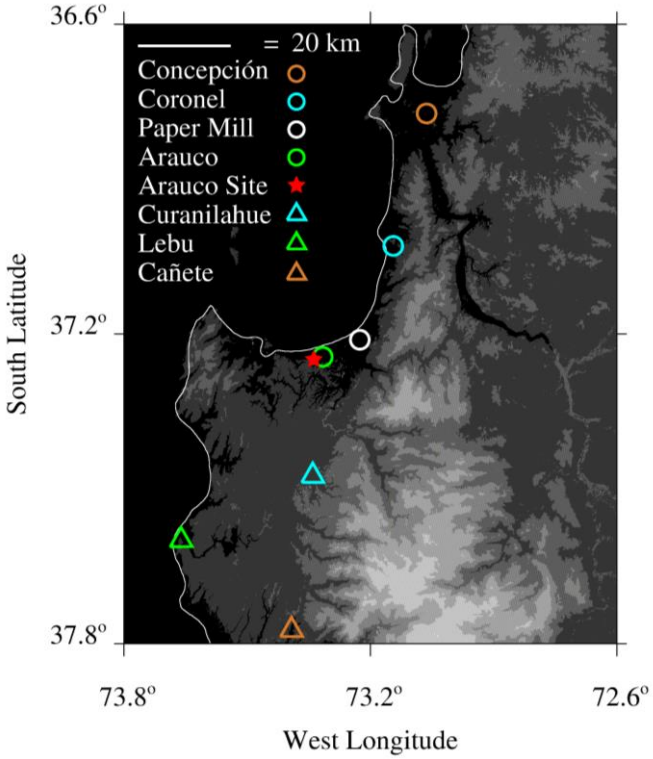

Fig. 1 – Central Chilean Coastal region and the location of Arauco Site where aerosol measurements were made during CCOPE. Altitude thresholds for the digital elevation map are at 0 m MSL, 50 m MSL, 250 m MSL, 500 m MSL, 750 m MSL, and 1000 m MSL.

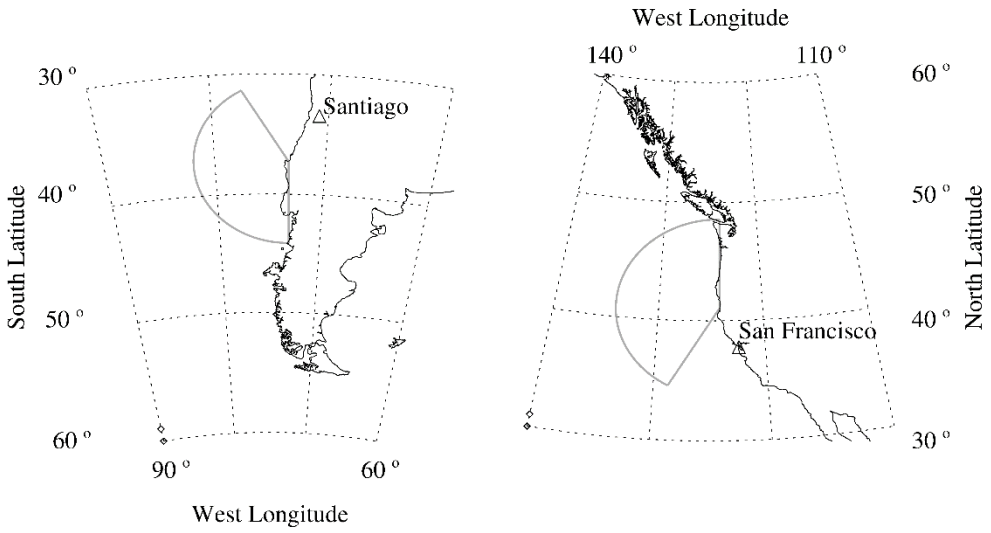

Fig. 2 - Clean sector chosen for Arauco (left, 180° to 330°) and the clean sector chosen for THD (right, 210° to 360°).

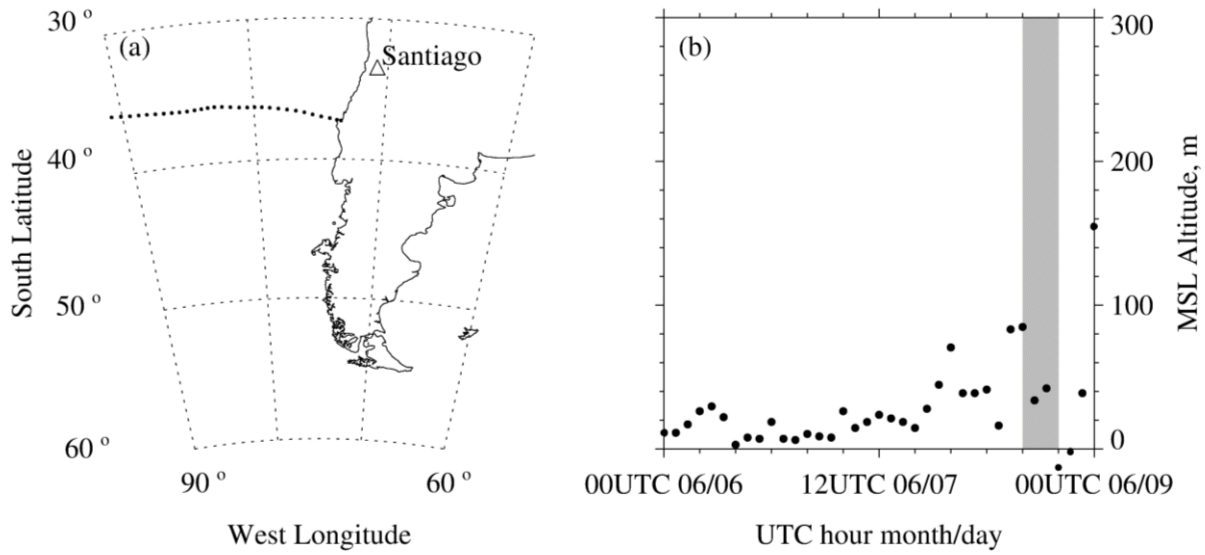

Fig. 3 - a) One of the 18 sea surface trajectories that arrived at the Arauco Site between 29 May to 28 June; this trajectory arrival occurred at 00 UTC June 9. Black dots are hourly output of the HYSPLIT model; however, for clarity, only every other 1-hr point is plotted. b) Hourly parcel MSL altitude vs time; however, for clarity, only every other 1-hr point is plotted. The averaged sea surface wind speed (U) was evaluated over the 12 to 18 UTC interval shown in gray. MSL altitude was calculated using the pressure output by HYSPLIT (parcel barometric pressure) and the ICAO equation for the Standard Atmosphere (1993). MSL altitude increases if a larger sea-level is pressure applied in the ICAO equation. This sensitivity is ~ 8 m / hPa.

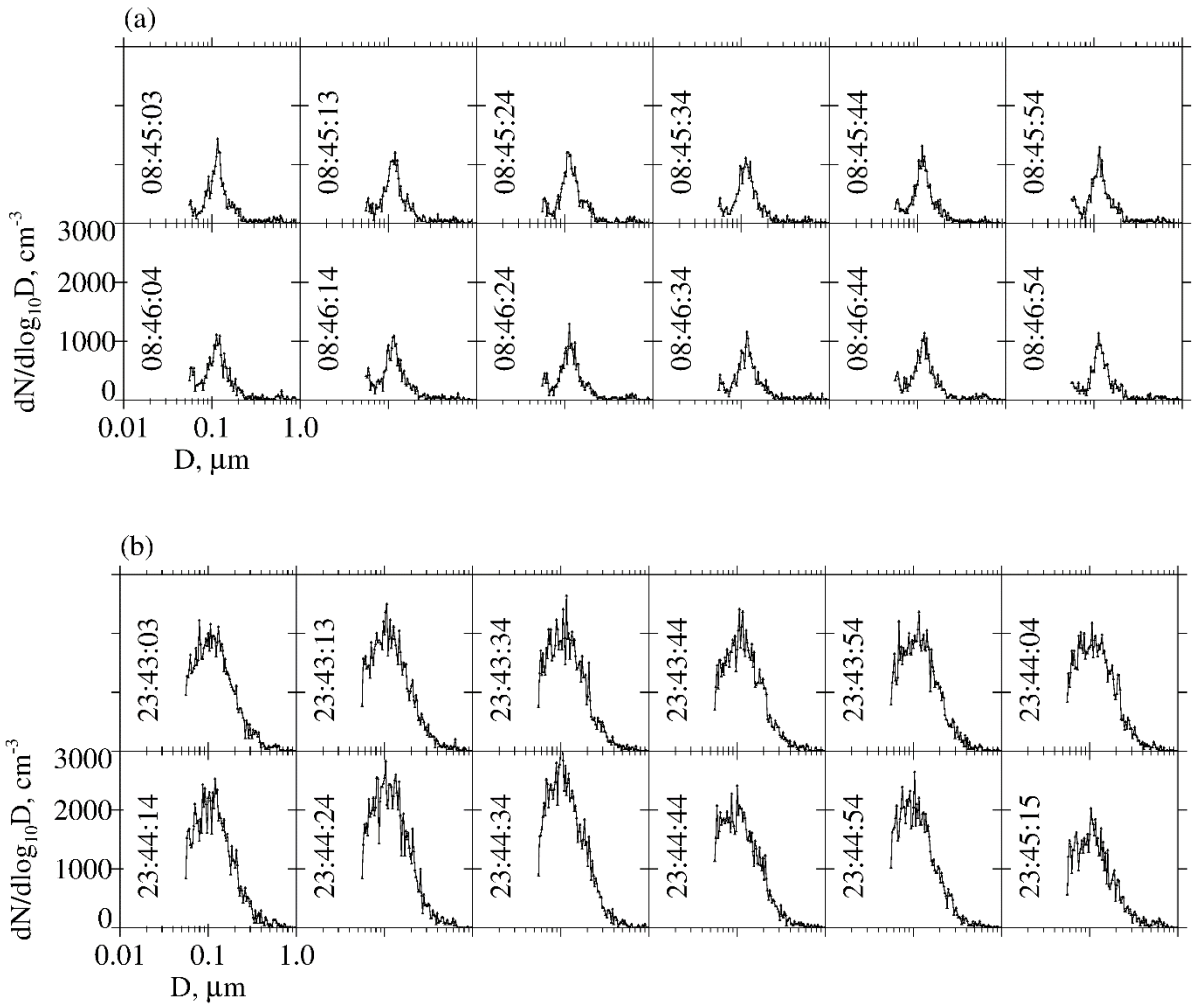

Fig. 4 - Consecutive ASDs recorded by the UHSAS at the Arauco Site. a) ASDs with a relatively small concentration (~ 300 cm^{-3}), a right tail of an Aitken mode (at ~ 0.06 µm), and an accumulation mode (at ~ 0.1 µm), in onshore-moving air on June 5, 2015. b) ASDs with a proportionately larger concentration (~ 1100 cm^{-3}), an accumulation mode (at ~ 0.1 µm), and no evidence of an Aitken mode, in air thought to be contaminated by continental sources (June 4, 2015). UTC time is written in each panel.

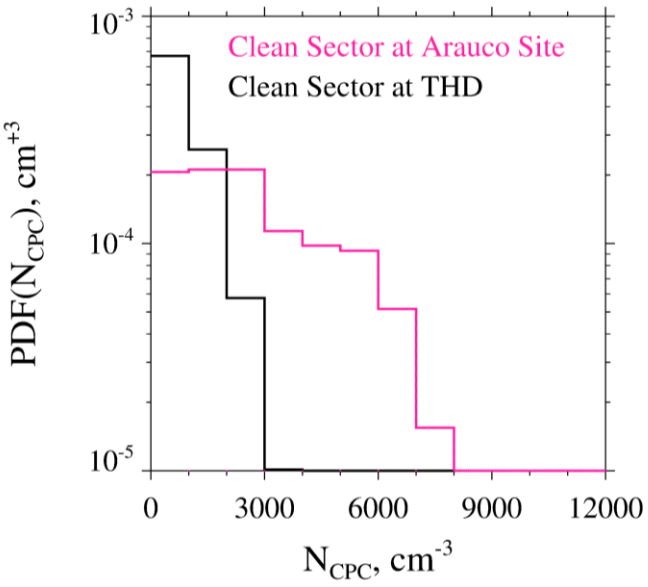

Fig. 5 - CPC concentration probability distribution functions for the Arauco Site and the THD.

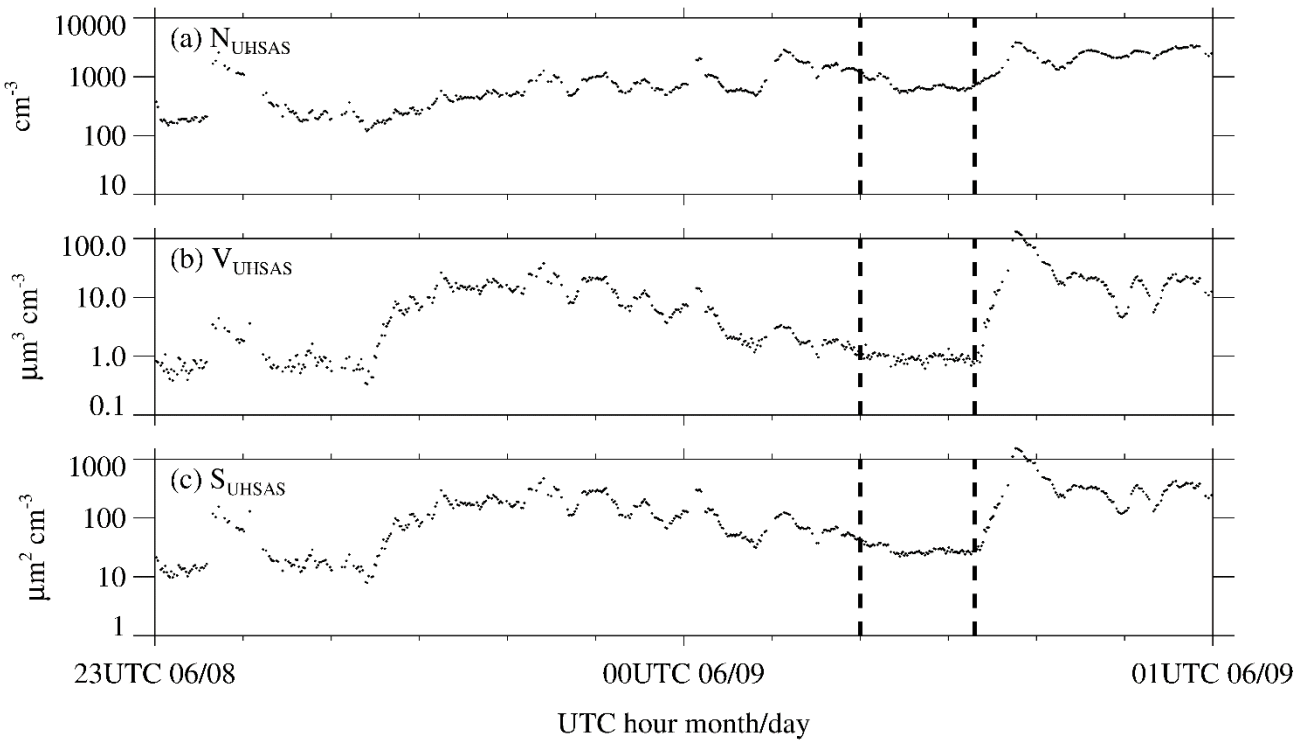

Fig. 6 – Aerosol properties centered on one of the 20 onshore trajectories that arrived at the Arauco Site between 29 May to 28 June. This trajectory arrival occurred at 00 UTC on June 9. a) UHSAS concentration; b) UHSAS aerosol volume; c) UHSAS aerosol surface area. Aerosol properties shown here were filtered using the procedure described in Appendix B. Vertical dashed lines mark the subset of the two-hour segment we picked (subjectively) as being representative of onshore-moving air that was relatively unaffected by continental aerosols compared to adjacent portions of the two-hour segment.

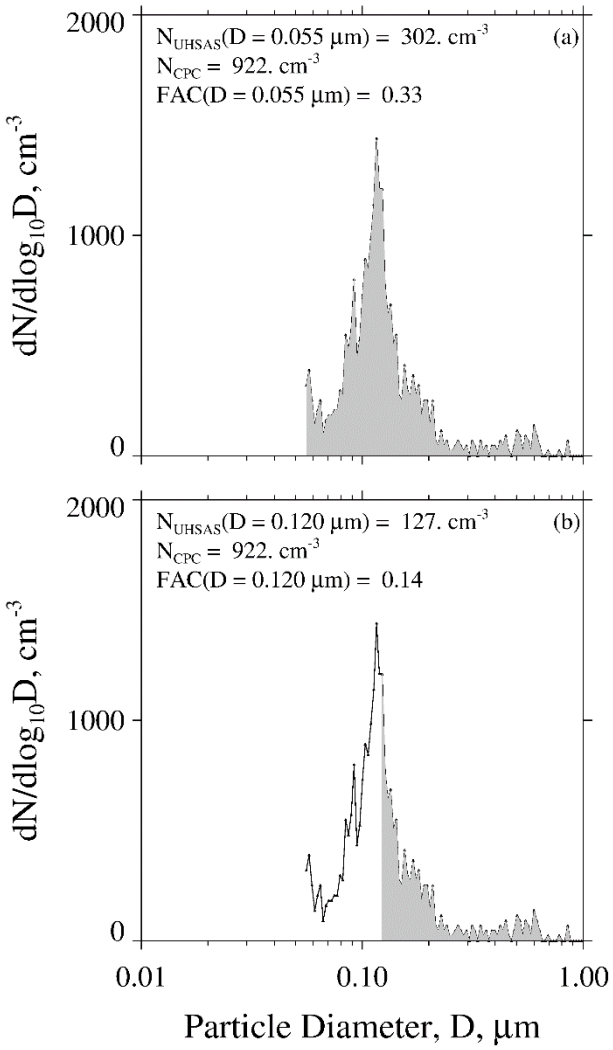

Fig. 7 - Two portrayals of the ASD recorded during CCOPE at 08:45:03 UTC June 5, 2015. This ASD is also plotted in Fig. 4a. Gray area in both panels represents the aerosol concentration integrated from the indicated lower-limit *D* to 1 µm. a) Figure legend has the size-integrated UHSAS concentration, calculated with lower-limit *D* set at 0.055 µm, the CPC concentration, and the fractional aerosol concentration (*FAC*). b) Figure legend has the size-integrated UHSAS concentration, calculated with lower-limit *D* in Eq. 2 set at 0.120 µm, the CPC concentration, and the fractional aerosol concentration (*FAC*).

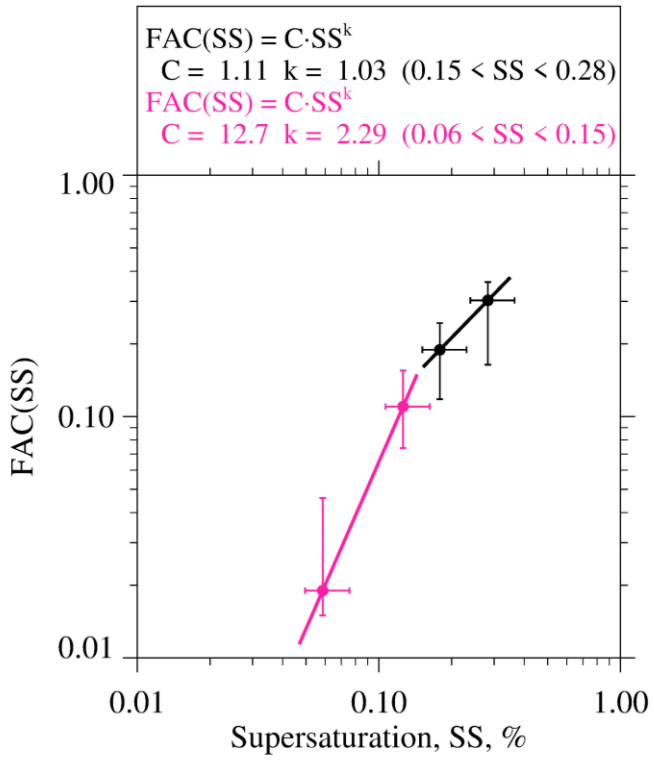

Fig. 8 - Parameterized CCN activity spectrum derived using CPC and UHSAS measurements from the 20 onshore trajectories that arrived at the Arauco Site between 29 May and 28 June 2015. Pink circles and the pink fit line are for lower-limit diameters set at 0.200 and 0.120 μm. Black circles and the black fit line are for lower-limit diameters set at 0.095 and 0.070 μm. Figure legend has power-law coefficients describing the parameterization; i.e., how *FAC* varies with *SS*.

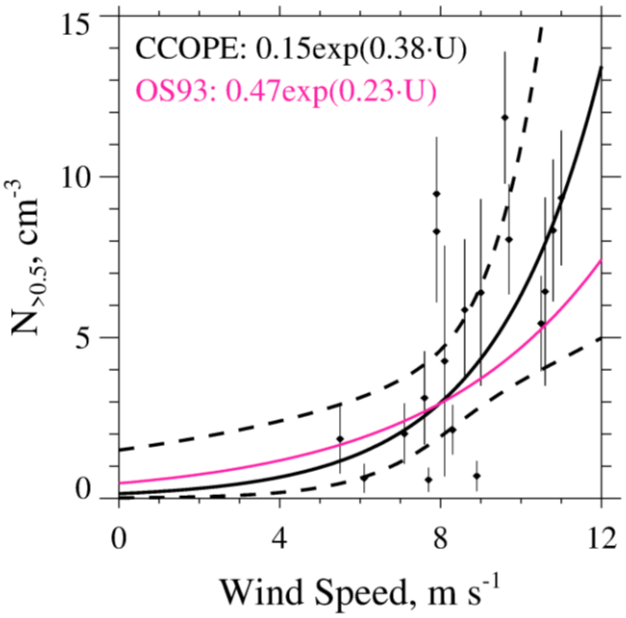

Fig. 9 – Averaged values of $N_{>0.5}$ (±1 standard deviation) vs HYSPLIT-derived averaged *U*s for the 18 sea surface trajectories that arrived at the Arauco Site between 29 May and 28 June 2015. The black curve is the fit of the CCOPE data; dashed curves above and below the black curves are 95% confidence intervals (Romano 1977; his Eq. 4.2.3.f). The pink curve is the fit reported by O'Dowd and Smith (1993) for 0.38 μm < *D* < 0.84 μm.

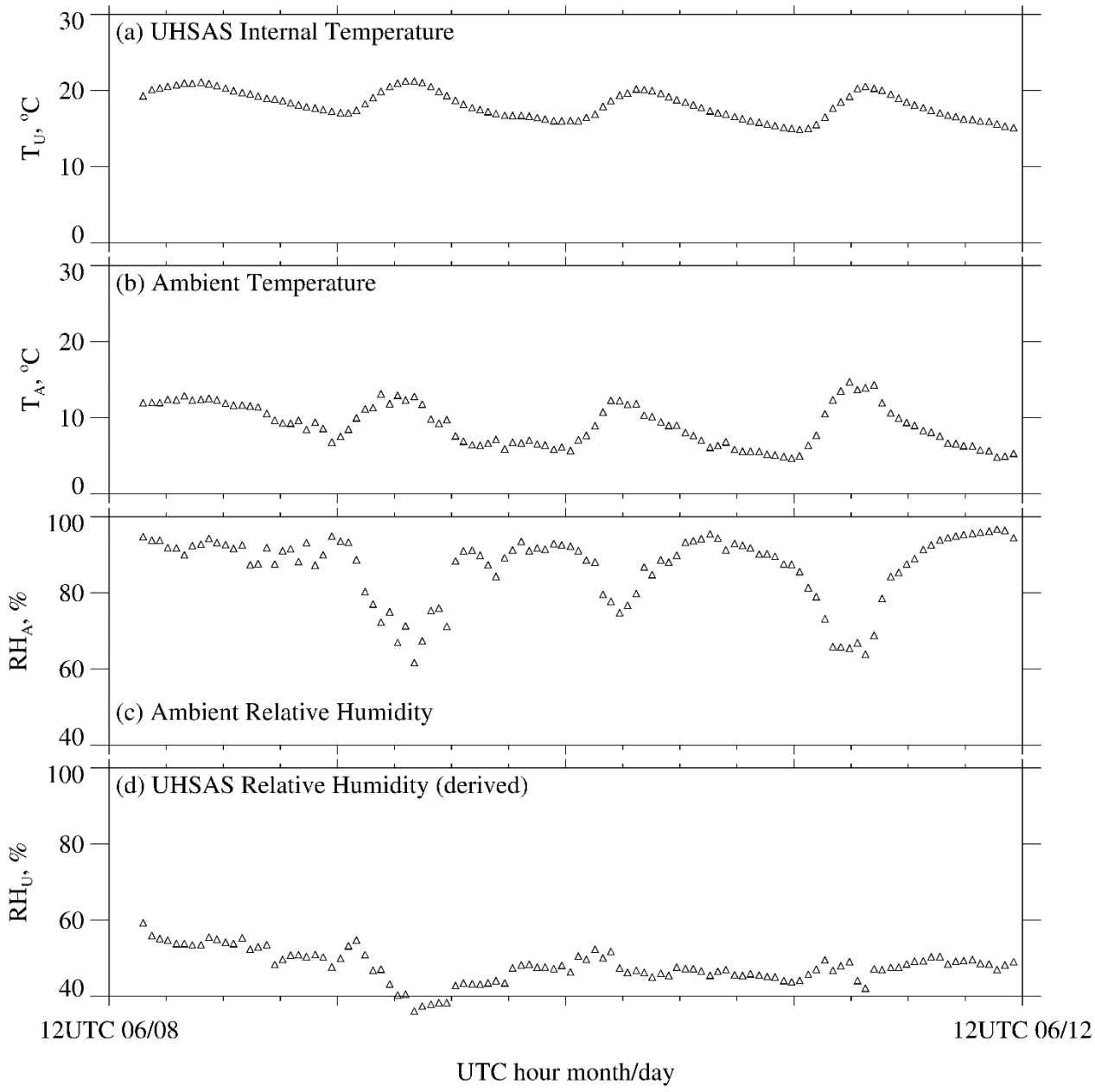

Fig. A1 – UHSAS internal temperature and ambient meteorological parameters at the Arauco Site over a four day period. a) Temperature inside the UHSAS; b) Temperature measured on the meteorological tower; c) *RH* measured on the meteorological tower; d) Derived *RH* inside UHSAS.

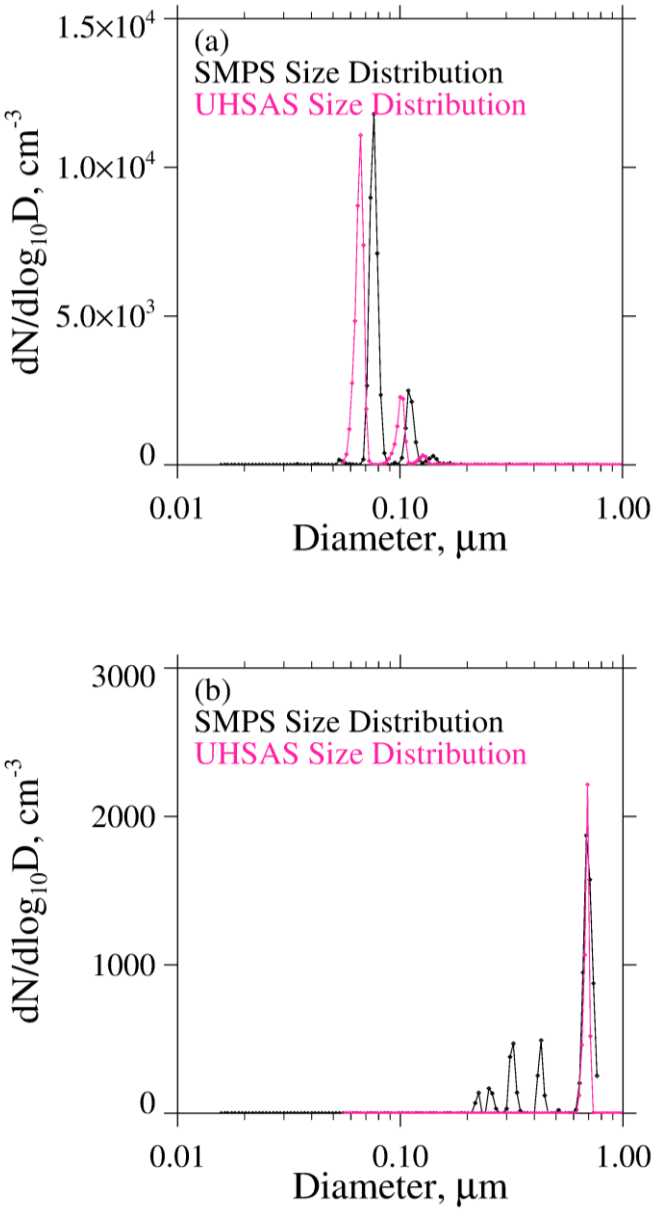

Fig. A2 – a) ASDs corresponding to mobility-selected D = 0.075 µm ammonium sulfate test particles. b) ASDs corresponding to mobility-selected D = 0.71 µm polystyrene test particles.

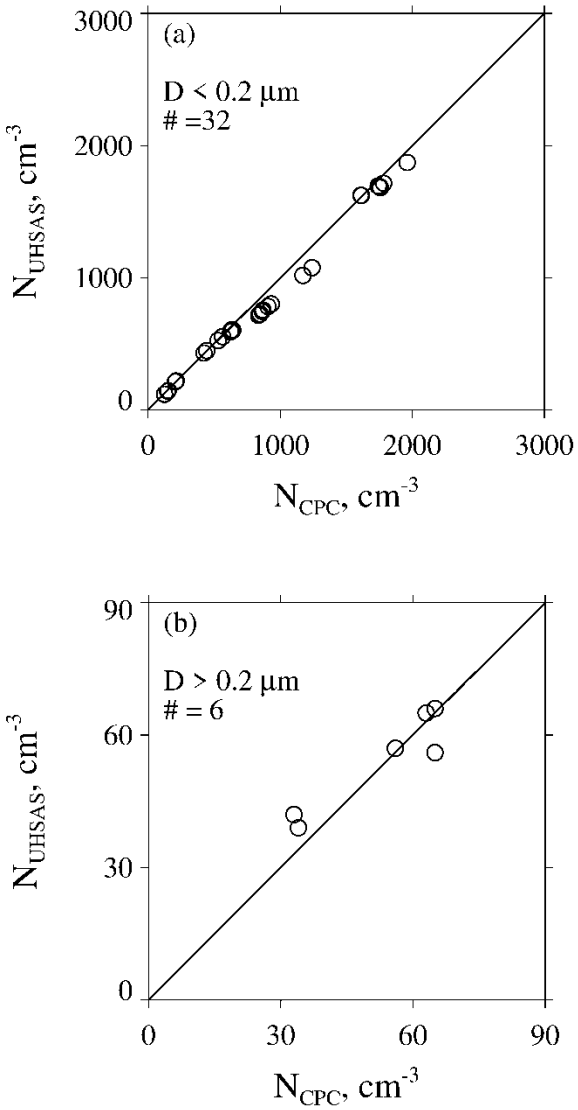

Fig. A3 - a) Size-integrated concentration from by the UHSAS versus concurrent laboratory measurements of concentration from the CPC. Results are for mobility-selected ammonium sulfate test particles with $D < 0.2$ μm. b) As in Fig. A3a but for mobility-selected ammonium sulfate test particles with $D > 0.2$ μm, and for mobility-selected polystyrene latex test particles with $D > 0.2$ μm.

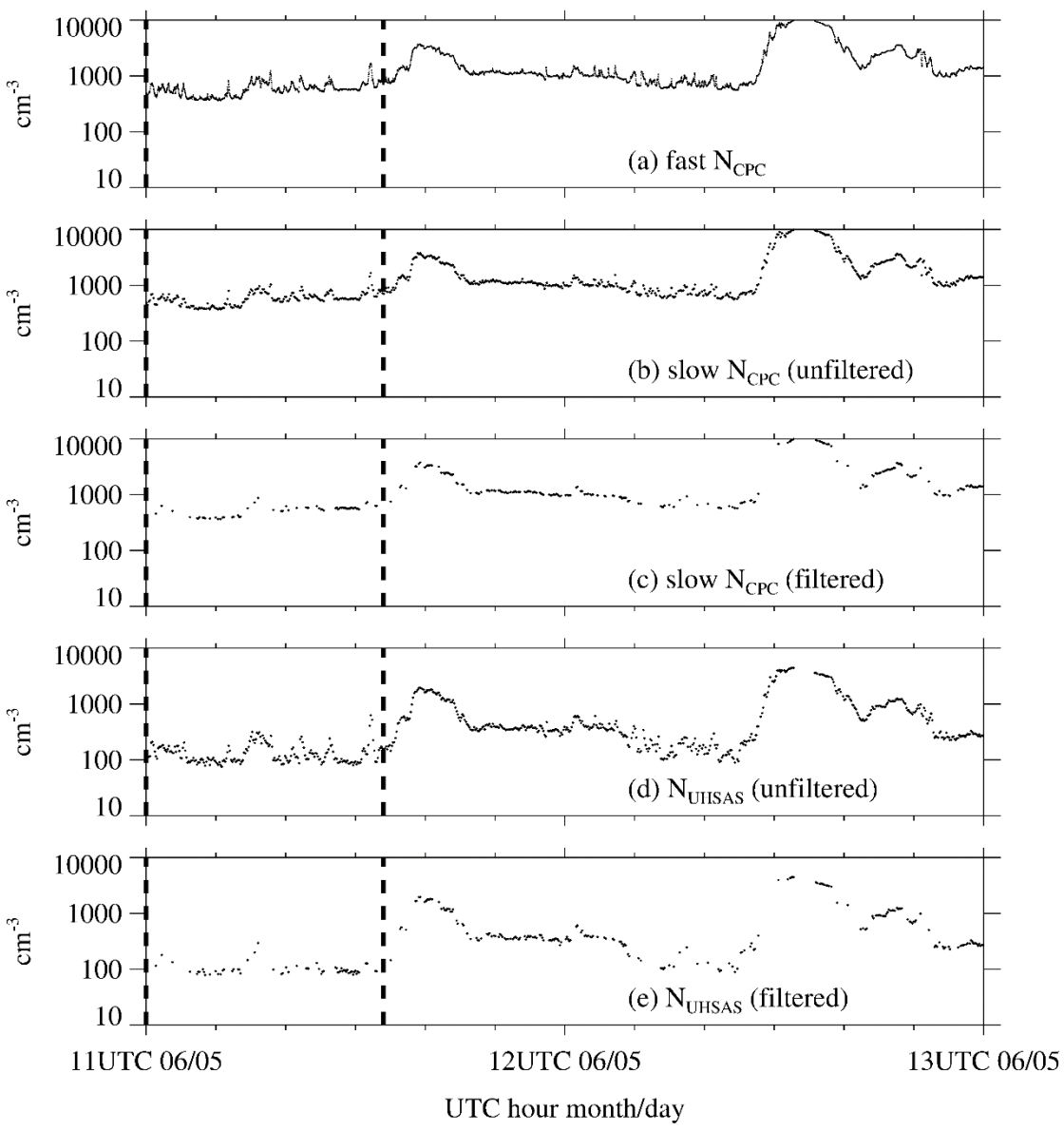

Fig. B1 - Demonstration of the numerical filter. Measurements from one of the 20 onshore trajectories that arrived at the Arauco Site between 29 May and 28 June. This trajectory arrival occurred at 12Z June 5. a) 1-s sampled CPC measurements; b) 10-s sampled CPC measurements; c) filtered 10-s CPC measurements; d) 10-s UHSAS measurements of size-integrated concentration; e) filtered 10-s UHSAS measurements of size-integrated concentration.